

# In-silico molecular transport via perivascular networks in the human intracranial space

Marius Causemann<sup>1</sup>, Miroslav Kuchta<sup>1</sup>, Rami Masri<sup>2</sup>, and Marie E. Rognes<sup>1,3,\*</sup>

<sup>1</sup>Department of Numerical Analysis and Scientific Computing, Simula Research Laboratory, Oslo, Norway

<sup>2</sup>Division of Applied Mathematics, Brown University, Providence, Rhode Island, USA

<sup>3</sup>K. G. Jebsen Centre for Brain Fluid Research, University of Oslo, Norway

\*meg@simula.no

## ABSTRACT

The mechanisms of intracranial solute transport are fundamental to human brain health, with alterations often linked to disease and functional impairment, and with distinct opportunities for personalized diagnostics and treatment. However, our understanding of these mechanisms and their interplay remains incomplete, in part due to the complexity of integrating insights across scales, between species and from different modalities. Here, we combine mixed-dimensional modelling, multi-modal magnetic resonance images, and high performance computing to construct and explore a high-fidelity in-silico model of human intracranial molecular transport. This model predicts the temporo-spatial spreading of a solute within an image-derived geometric representation of the subarachnoid space, ventricular system and brain parenchyma, including networks of surface perivascular spaces (PVSs). Our findings highlight the significant impact of cerebrospinal fluid (CSF) production and intracranial pulsatility on tracer enrichment following intrathecal tracer injection. We demonstrate that low-frequency vasomotion induces moderate CSF flow in surface PVS networks which substantially enhances tracer enrichment, and that impaired enrichment is a direct natural consequence of enlarged surface PVSs. This openly available technology platform thus provides an opportunity for integrating separate observations on diffusion in neuropil, vascular dynamics, intracranial pulsatility, CSF production, and efflux, and for exploring drug delivery and clearance in the human brain.

## Introduction

The mechanisms underlying molecular transport within the intracranial space are fundamental to human brain health and function. Neurodegenerative diseases such as Alzheimer's, Parkinson's, and Huntington's disease are all associated with abnormal accumulation of protein aggregates together with alterations in transport and clearance characteristics<sup>1–4</sup>. Moreover, sleep and conversely sleep-deprivation play a definite yet enigmatic role in modulating molecular enrichment<sup>5–9</sup>. In the last decade, established theories have been challenged by new findings revealing a greater degree of on molecular movement and exchange<sup>10–14</sup>, as well as substantial variability in enrichment and clearance including substantial variability<sup>5–9</sup> between individuals and between patient cohorts<sup>7,15–17</sup>. These observations provide distinct opportunities (and challenges) for personalized medicine e.g. for tailored intrathecal delivery of chemotherapy<sup>18</sup> chemotherapies<sup>18</sup> such as methotrexate in acute lymphoblastic leukemia patients<sup>19</sup>, and for early diagnostics of impaired brain clearance<sup>20,21</sup>. In spite of their importance, our understanding of these mechanisms is incomplete with open challenges and significant debate – in part relating to the translation of knowledge between scales, species, experimental protocols, clinical cohorts, and individuals.

Perivascular pathways along the brain surface and within the brain parenchyma have long been hypothesized to serve a designated role in this context<sup>10,22–28</sup>. Recently, Eide and Ringstad<sup>29</sup> and Yamamoto et al<sup>30</sup> demonstrated that perivascular spaces (PVSs) define preferential pathways for molecular transport in humans, with delayed periarterial enrichment in dementia subtypes<sup>29</sup>. Perivascular flow of cerebrospinal fluid (CSF) clearly contributes to this transport, and is inherently associated with vascular pulsations<sup>31–36</sup>. Fluid mechanics considerations point at intracranial pressure differences and shorter wavelength vascular wall pulsations as drivers of directional net flow and convection in the PVS<sup>37–42</sup>, while longer waves such as the pulse wave primarily contribute to oscillatory flow and dispersion<sup>43–48</sup>. In the bigger picture, CSF is produced by the choroid plexus<sup>49–51</sup>, pulsates through the ventricular system, cisterns, and subarachnoid space (SAS) in synchrony<sup>52–59</sup> association with cardiac, respiratory, and neural waves<sup>16,52–59</sup>, and drains via the dural sinuses, meningeal lymphatics, cranial nerves, or other efflux pathways<sup>13</sup>. However, how these physiological factors and physical mechanisms integrate to enhance or impair human intracranial molecular transport over larger spatial scales and longer time scales remain unknown. A related key question is to what extent surface PVSs are separated from the SAS by structural barriers<sup>23,29,60–65</sup>, and in turn to what extent such structural compartmentalization is a prerequisite for effective perivascular transport.

In this study, by leveraging geometric model reduction and mixed-dimensional modelling<sup>66</sup>, structural magnetic resonance (MR) images<sup>67</sup>, and high performance computing, we introduce an integrated computational model of intracranial molecular enrichment and clearance transport. Focusing on the interplay between perivascular pathways, pulsatility and CSF flow dynamics, the model predicts the temporal evolution and spatial distribution of a solute concentration within a detailed geometric representation of the human SAS and ventricular system, in networks of surface PVSs and (i.e. those surrounding arteries and veins in the SAS), and in the brain parenchyma. In terms of transport dynamics, we account for heterogeneous diffusion, dispersive mixing induced by cardiac and respiratory pulsatility in the CSF spaces and PVSs, convective fluid flow driven by CSF production and peristaltic pumping, as well as solute exchange and clearance across semi-permeable membranes. Comparing with glymphatic MRI studies <sup>11,15,68</sup><sup>11,15,29,68</sup>, the in-silico predictions accurately represent molecular tracer enrichment patterns, timing and intercompartmental distributions. This open platform<sup>69</sup> thus provides a technological opportunity for qualitatively and quantitatively exploring key open questions relating to molecular movement within the human brain environment such as the role of pulsatility, perivascular pathways, structural compartmentalization, or morphology.

By exploring this high-dimensional parameter space, we propose that the balance between CSF production and intracranial pulsatility is key to shaping the large-scale features of intracranial enrichment patterns, with the potential to span a wide range of individual and cohort variability. Moreover, we predict that CSF production, cardiac- and respiratory pulsatility is not sufficient to explain early perivascular enrichment, but that fluid flow induced by low-frequency vasomotion in surface periarterial spaces (on the order of 10 μm/s) is sufficient, even in the absence of a structural compartmentalization of the PVS. Conversely, enlarged PVSs in the SAS will cause a substantial reduction in cardiac- and vasomotion-driven flow velocities, strongly delay perivascular transport, and thus impair intracranial enrichment. These findings transfer, reconcile, integrate and extend insights from clinical, experimental, and theoretical studies, and lay a new foundation for provide a framework for future in-silico studies of personalized intrathecal drug delivery and brain clearance.

## Results

### In-silico predictions of intracranial molecular enrichment and clearance transport after intrathecal injection

Using previously published multi-modal magnetic resonance imaging (MRI) data<sup>67,70–73</sup>, we construct a multiscale computational representation of the human intracranial compartments consisting of the CSF spaces and brain parenchyma as three-dimensional (3D) domains and with the PVSs surrounding major surface arteries and veins as embedded networks of topologically one-dimensional (1D) curves (Figure 1A–B). We consider a solute concentration field, varying in space and time, in the 3D domains and in the PVS networks, and assume that the solute can cross between these compartments through semi-permeable membranes. As the drivers and modes of intracranial transport are under substantial debate<sup>13,14,74–76</sup>, our first target is to establish a baseline model accounting for a reasonably conservative set of mechanisms and their integrated effect over a timescale of several minutes to a few days. To this end, we assume that the solute will (i) diffuse within all compartments, with diffusivity depending on the effective properties of the relevant medium<sup>77</sup>; (ii) experience significant dispersive effects due to the pulsatile flow of CSF induced by the cardiac and respiratory cycles<sup>44,47,56,78</sup>; and (iii) be convected by a (small) net flow of CSF resulting from production in the choroid plexus with CSF efflux across the upper convexity<sup>79</sup> and from the peristaltic pumping effect of pulse wave pulsations in surface periarterial spaces<sup>34,41</sup>. Mathematically, this model is represented by a mixed-dimensional system of coupled time-dependent partial differential equations<sup>66</sup>, which we solve numerically with high accuracy using a mass-conserving finite element scheme and the FEniCS finite element software<sup>80,81</sup> (see Methods). The computational framework and associated software are all openly available<sup>69</sup>.

Simulating a glymphatic MRI protocol<sup>11,15,29</sup> (Figure 1C), we then predict the spreading of 0.5 mmol intrathecally injected Gadobutrol after its appearance at the craniocervical junction, represented by tracer inflow across the spinal SAS boundary over the first two hours (Figure 1D–E). After one hour, the in-silico tracer moves upwards in the SAS frontally of the brainstem, and quickly reaches the supratentorial regions. Here, it spreads both posterior through the quadrigeminal cistern and the longitudinal fissure, and anteriorly through the outer SAS, reaching the top of the cerebral cortex after around 12 hours. After 24 hours, the tracer covers most of the brain surface (with the exception of some posterior regions) and has penetrated substantially into the parenchymal tissue. This pattern is reflected in the mean tracer concentrations in each compartment, where the CSF space reaches its peak of 1.4 mmol/l after 2 hours, followed by the arterial PVS concentration peak (2.9 mmol/l after 4 hours) (Figure 1F). While the mean concentrations in these compartments drop soon after peaking, the parenchymal tissue slowly enriches with tracer over the first 24 hours, with a final value of 0.3 mmol/l. Overall, about 40% of the total amount of tracer remains in the cranium 24 hours post-injection, with the largest share in the CSF (53%), followed by the parenchyma (35%), the venous PVS (8%) and the arterial PVS (5%) (Figure 1G).

### Reduced CSF pulsatility strongly shifts intracranial enrichment patterns

The tracer enrichment patterns observed clinically after intrathecal injection of contrast differ substantially between subjects and between pathological conditions<sup>7,15–17</sup>. These neurological conditions are also associated with alterations in the pulsatile

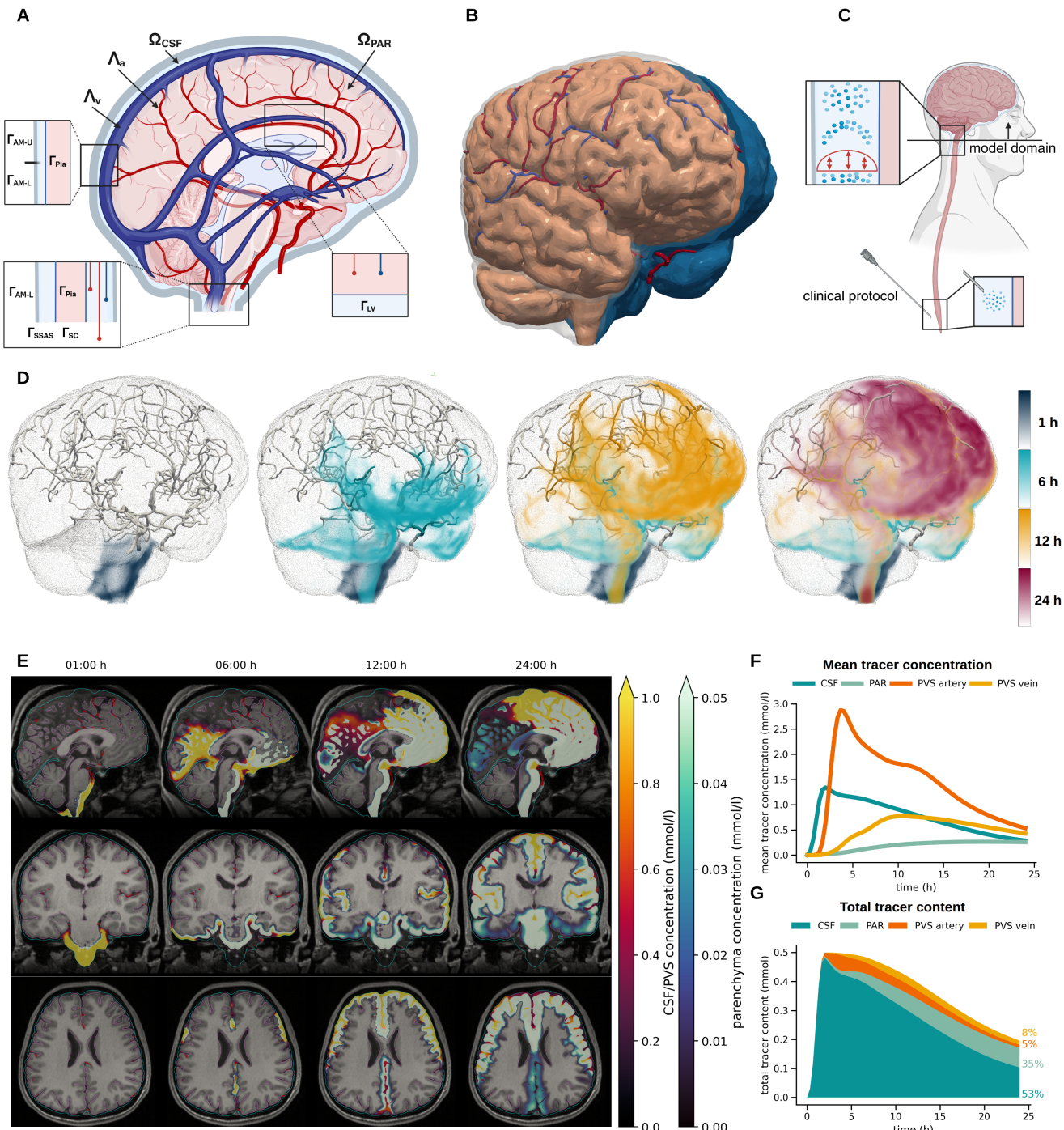


**Figure 1. In-silico modelling of molecular enrichment and clearance of the PVS, SAS and parenchyma. In-silico modelling of tracer transport in the PVS, SAS and parenchyma.** A) Illustration of the model geometry including the CSF-filled spaces (ventricles and SAS)  $\Omega_{CSF}$ , the parenchyma  $\Omega_{PAR}$  and the PVS surrounding arteries  $\Lambda_{artery}$  and veins  $\Lambda_{vein}$ , as well as their interfaces and boundaries; B) 3D rendering of the computational geometry: the parenchyma, CSF (clipped, blue), arterial network (red), and venous network (blue); C) illustration of model representation of the intrathecal tracer injection protocol; D) in-silico predictions of tracer concentration after 1, 6, 12, and 24 hours (opacity increasing linearly from 0 to 2 mmol/l); E) sagittal, coronal and axial view of in-silico tracer concentrations overlayed on T1-weighted MR image after 1, 6, 12 and 24 h (low concentrations transparent, pial surface in pink, arachnoid membrane in cyan, and arteries in dark red); F) average tracer concentration in each compartment over the first 24 h; G) total amount of tracer in each compartment over the first 24 h.

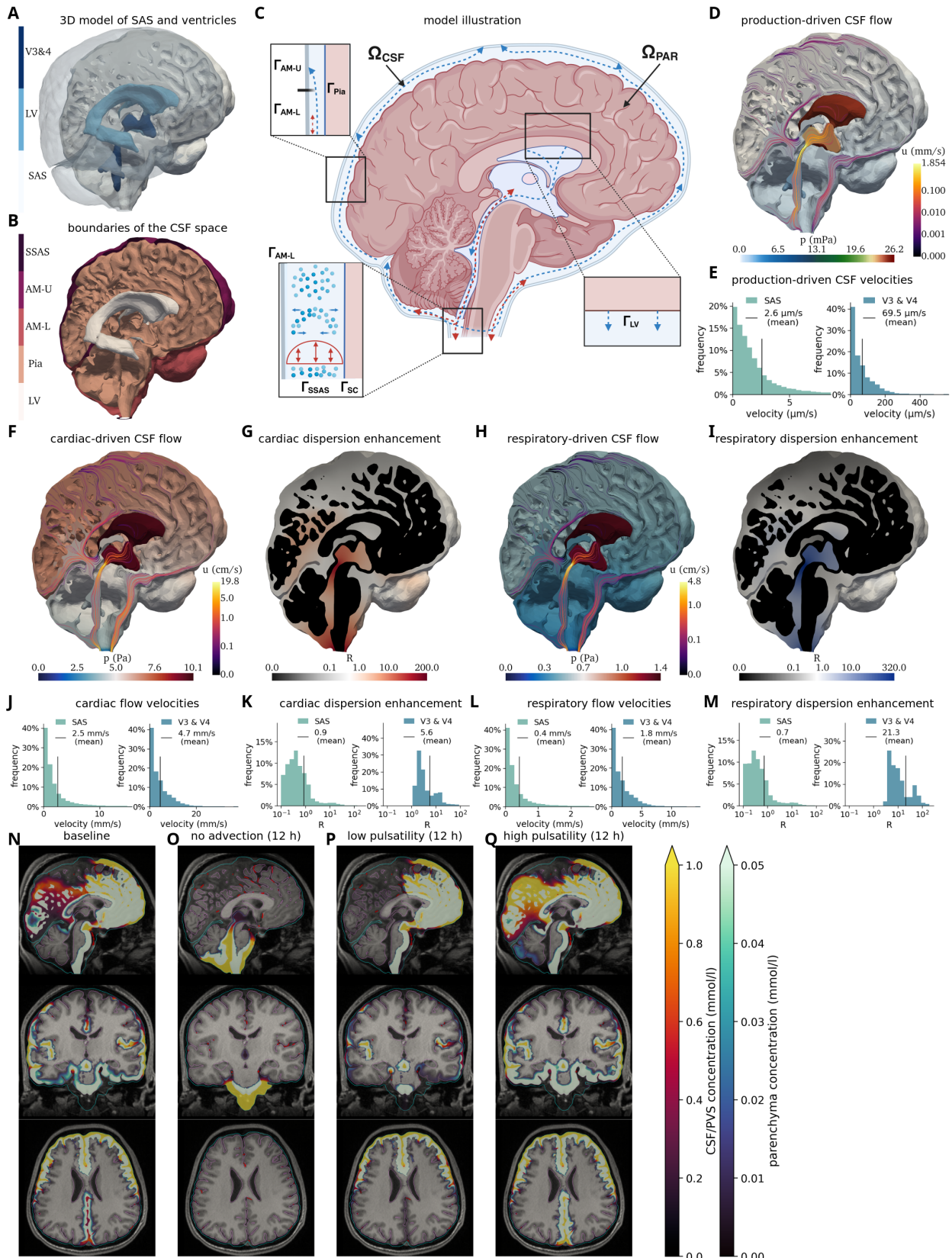


**Figure 2. The balance between CSF pulsatility and production shapes molecular enrichment patterns. The balance between CSF pulsatility and production shapes tracer enrichment patterns.** A) CSF spaces: the third and fourth ventricle (V3&4), lateral ventricles (LV) and SAS; B) Boundaries and interfaces: the spinal subarachnoid space (SSAS), upper and lower arachnoid membrane (AM-U and AM-L), pia (Pia) and lateral ventricles (LV); C) Schematic of the CSF flow model; D) CSF flow induced by CSF production with outflow allowed across the upper convexity (AM-U);

**Figure 2. (cont.)** E) Histograms of the production-induced CSF velocities in the SAS and third and fourth ventricle (V3 & V4) in terms of the relative frequency of the mean flow speed in each computational cell weighted by its volume; F) CSF flow induced at peak systolic blood inflow; G) Cardiac-induced dispersion factor  $R_c$ ; H) CSF flow induced at peak respiratory expansion; I) Respiration-induced dispersion factor  $R_r$ ,  $D = (1 + R_c + R_r)D^{\text{Gad}}$ ; J–M): Histograms of the cardiac-induced flow velocities (J), cardiac-induced dispersion factors (K), respiratory flow velocities (L), respiratory dispersion factor (M); N–Q): sagittal, coronal and axial planes of tracer concentration after 12h for different model variations: baseline (N), no CSF production (O), low dispersion (P), and high dispersion (Q).

flow of CSF in the ventricular system and SAS<sup>16</sup>. Clearly, key physiological factors such as cardiac pulsatility and respiration easily differ between individuals and between both pathological and physiological states. We therefore next asked to what extent – and how – variations in CSF pulsatility would affect the intracranial enrichment characteristics.

For the CSF dynamics in our baseline model, we combine the net contribution to CSF flow induced by CSF production with the integrated dispersive effects of cardiac and respiratory pulsatile CSF flow (Figure 2A–C). **Impose Beginning with the advective, net flow field driven by CSF production, we impose** a constant CSF **production inflow** of 400 ml/day across the surface of the lateral ventricles, **while** **Simultaneously** allowing for efflux across the upper convexity, **yields** a total CSF pressure drop of 26 mPa (0.00020 mmHg) (Figure 2D) with a maximum flow velocity of 1.85 mm/s (in the aqueduct) and a mean velocity in the SAS of 2.6 µm/s (Figure 2E). **To Next, to** examine the dispersive effects of pulsatile CSF flow, we employ the theory of shear-augmented dispersion together with computational fluid dynamics to determine a dispersion factor  $R$  enhancing the effective solute diffusivity (see **Methods**). **For Supplementary information S1.3 for a complete description**). **To estimate** the cardiac contribution, we compute the **steady state** CSF pressure and flow fields at peak systolic blood inflow, **corresponding to a**. **Modelling the** reduction in CSF space volume **at a total corresponding to peak systolic conditions, we assume a total inflow** rate of 6 ml/s<sup>57,82</sup> in the SAS **across its outer surface** and 0.31 ml/s across the lateral ventricle surface<sup>56</sup>. This scenario sets up a pressure drop of 10 Pa (0.075 mmHg) between the lateral ventricles and the spinal SAS and a maximum flow velocity of 19.8 cm/s (Figure 2F, J). Assuming a cardiac frequency of 1 Hz, we infer that this cardiac-induced pulsatile CSF flow increases the effective diffusion by more than two orders of magnitude in the aqueduct and near the cisterna magna, but has little effect ( $R < 1$ ) in most of the SAS (Figure 2G, K). For the respiratory contribution, we employ the same methodology, but with a total rate of 1 ml/s<sup>83</sup> in the SAS and 0.121 ml/s<sup>84</sup> in the lateral ventricles, yielding a respiratory peak flow volume of 1.121 ml/s at the craniocervical junction. While the resulting flow velocities are only about one fourth of their cardiac-induced counterparts (Figure 2H, L), respiratory dispersive mixing reaches a factor of up to 320 due the lower respiratory frequency of 0.25 Hz (Figure 2I, M).

Now, to examine how CSF pulsatility affects the **tracer** enrichment patterns, we consider three variations of the baseline: (i) no CSF production, (ii) reduced pulsatility and thus decreased dispersion( $0.1 \times R$ ), and (iii) higher pulsatility with increased dispersion( $10 \times R$ ). **We computed the reduced and increased pulsatility scenarios by halving and doubling the inflow rates associated with both cardiac and respiratory pulsations, which changed the dispersion factors by  $0.25 \times$  and  $4 \times$ , respectively.** **Note that behaviour directly reflects the nature of our model: Stokes flow is linear in its inflow boundary conditions, and the diffusion enhancement factor is quadratic in the predicted pressure gradient.** Without CSF production, transport is considerably delayed (Figure 2N, O). Even after 12 hours, tracer remains in the subtentorial regions around the cerebellum, the brain stem and in the surrounding CSF. Interestingly, the lack of CSF production instead allows tracer to travel upwards through the ventricular system, reaching the third ventricle after around 12 hours. On the other hand, if the CSF pulsatility is reduced, we observe rapid transport towards the upper convexity of the cranium, as in the baseline model, but the tracer spreads exclusively within the anterior regions (Figure 2P). This feature can be attributed to the CSF flow bifurcation posterior to the ambient cistern (Figure 2D): without sufficient diffusion, the tracer is unable to cross into the posterior SAS. Indeed, with higher dispersion, the tracer moves through the quadrigeminal cistern and further upwards into the longitudinal fissure, with also enrichment of the cerebellum (Figure 2Q).

#### 124 **Perivascular flow shapes and accelerates molecular enrichmenttransport**

The PVSs are recognized across species as critical pathways for solute transport in and around the brain, and thus as potential targets for enhancing brain drug delivery and metabolic waste clearance. However, whether CSF flows more rapidly in PVSs and what the forces and mechanisms required to drive such flow are, remain as key points of debate<sup>14,28</sup>. Motivated by experimental observations in animal models<sup>10,32–34</sup>, there is now a remarkable body of literature on modelling perivascular fluid flow and transport<sup>37–48</sup>. Here, we ask how these proposed mechanisms would translate from idealized geometries to human vascular networks and moreover, evaluate their integrated effect in the context of intracranial solute transport.

Our periarterial network extends from the internal carotid arteries and basilar artery through up to 18 bifurcations to reach upstream network ends located within the SAS or up to 6 mm inside the parenchyma (Figure 1A–B, Figure 3A) and includes

major surface arteries of radius 0.5–1.4 mm. Due to imaging limitations, the network primarily covers the supratentorial regions, with the lowest network point located approximately 4 cm above the craniocervical junction. Imposing the pressure field induced by CSF production at the periarterial network ends induces slow steady CSF flow of variable direction in these PVSs, with an average velocity of 0.08  $\mu\text{m/s}$  (antegrade) and a maximum velocity of 0.55  $\mu\text{m/s}$  (Figure 3B). On the other hand, traveling waves of arterial wall motion (Figure 3C), such as the pulse wave or other vasomotion<sup>9,85–88</sup>, also induce net directional flow in the PVS<sup>40–42,46,89</sup> – of magnitude and direction depending on the amplitude, frequency, and length of the waves and the characteristics of the perivascular network<sup>41</sup>. Applying a semi-analytic model of the net flow induced by peristalsis in perivascular networks<sup>41</sup> (see Methods), we estimate that the cardiac pulse wave alone, traveling at a frequency of 1 Hz with a wavelength of 2.0 m and a 1% wall displacement<sup>90</sup>, will induce mainly antegrade PVS flow with an average net velocity of 0.92  $\mu\text{m/s}$  while reaching up to 7.31  $\mu\text{m/s}$  near larger, ventral vessels such as the MCA (Figure 3D,E). The same theory predicts that strong ultraslow vasomotions, if traveling antegrade at 0.1Hz with a wavelength of 0.02 m and a 10% displacement<sup>88</sup>, will induce both retrograde and antegrade net PVS flow with an average velocity of 13.05  $\mu\text{m/s}$  and maximum velocity 54.44  $\mu\text{m/s}$  (Figure 3D,F).

We study the effect of such rapid PVS flow on intracranial molecular enrichment transport by comparing the more conservative baseline model and a high PVS flow model, where the former still includes the net flow contributions from CSF production and the cardiac pulse wave, while the latter additionally includes the ultraslow vasomotion contribution. In both models, tracers were first observed at the basal artery after 48 minutes (Figure 4A), defined by their first-time arrival (FTA), the time at which the concentration first exceeds 0.1 mmol/l. At all upstream locations along the middle cerebral arteries (MCAs) and anterior cerebral artery (ACA), we found substantially reduced FTAs with higher PVS flow (Figure 4B), up to 2.5 hours earlier in the left M2 segment of the MCA. PVS concentrations peaked before the surrounding tissue (0:48h vs 1:12h at the MCA and 1:00h vs 1:48h at MCA2) with high PVS flow, while these peaks occurred nearly simultaneously in the baseline model. The earlier appearance and the delay in time-to-peak between the PVS and surrounding tissue clearly indicates the directionality of tracer enrichment – it first arrives in the PVS and subsequently spreads into the tissue and SAS (Figure 4C, D), and especially so with higher PVS flow. These observations also hold on an aggregated level: computing the total amount of tracer in the PVS as a function of the distance to the arterial network roots, we find accelerated tracer transport with higher PVS flow, especially at earlier time points (2–9 hours) (Figure 4E). Moreover, differences in tracer transport along the PVS translate to altered enrichment patterns on the whole-organ scale. For instance, after 4–6 hours, the faster-moving tracer in the PVS is clearly visible in the space adjacent to the PVS of the ACA, MCA, and other arteries (Figure 4G). In contrast, there are no clear signs of early enrichment surrounding the PVS in the baseline model (Figure 4F).

A natural question is whether early PVS enrichment could be the result of increased dispersion rather than net flow in the PVS<sup>43,44,47,87</sup>. Interestingly, even increasing the dispersion factor by 100× in the PVS, induced only minor changes in the global spreading rate compared to the baseline (Figure 4F, H), thus indicating a negative answer to this question.

## Structural versus functional compartmentalization of perivascular spaces

Human and rodent observations indicate that tracers concentrate in perivascular spaces surrounding the pial and subarachnoid vasculature<sup>23,29,33,34,61,91</sup>. However, it remains unclear whether such enrichment patterns necessitate a structural barrier, such as a membrane with limited permeability, or if the patterns could result from enhanced flow or mixing in these areas alone. We therefore next investigate how the permeability of the interface between the PVS and the surrounding CSF affects tracer enrichment around the major arterial trunks (Figure 5A–B). To this end, we compare models with high and low permeabilities, representing a highly permeable PVS-CSF interface (functional compartmentalization) and a less permeable interface (structural compartmentalization), respectively. For the low permeability model, we set the permeability to  $3.8 \cdot 10^{-7} \text{ m/s}$ , consistent with previous estimates for the endfoot sheath surrounding penetrating arterioles<sup>92</sup>, which we consider to be a lower bound for the surface PVS-CSF permeability. For the high permeability model, we increase this permeability by a factor of 100. For We emphasize that, for both scenarios, we consider the high PVS flow regime as examined in the previous section.

At the basal artery (BA), tracer appears within one hour in the surrounding CSF in both models (Figure 5C, E). With a more permeable PVS-CSF interface, tracer quickly crosses from the CSF into the PVS, resulting in similar peak concentrations of 25 mmol/l in the PVS and at its outer surface, while values up to 50 mmol/l are attained in the vicinity. In contrast, the low permeability model exhibits substantially lower perivascular tracer enrichment, with a maximum concentration of 10 mmol/l after approximately two hours. For the middle cerebral arteries (MCA-R and MCA-L), tracer appears first in the PVS in both models (Figure 5D, E), though with higher concentrations in the high permeability model (up to 24 mmol/l). We also observe that the higher permeability allows the tracer to leak out of the PVS and spread within the Sylvian fissure to a greater extent. With a small delay, more tracer appears via the CSF pathway (Figure 5D). At the anterior cerebral artery (ACA-A2), the first tracer arrival in the PVS occurs after 3 hours, with a peak at 5 hours. The concentration peak in the PVS is tailed by a higher peak in the CSF (Figure 5E), indicating tracer arrival through a second pathway; i.e., directly through the CSF-filled space outside of the PVS. Similar patterns are observed for ACA-A3.

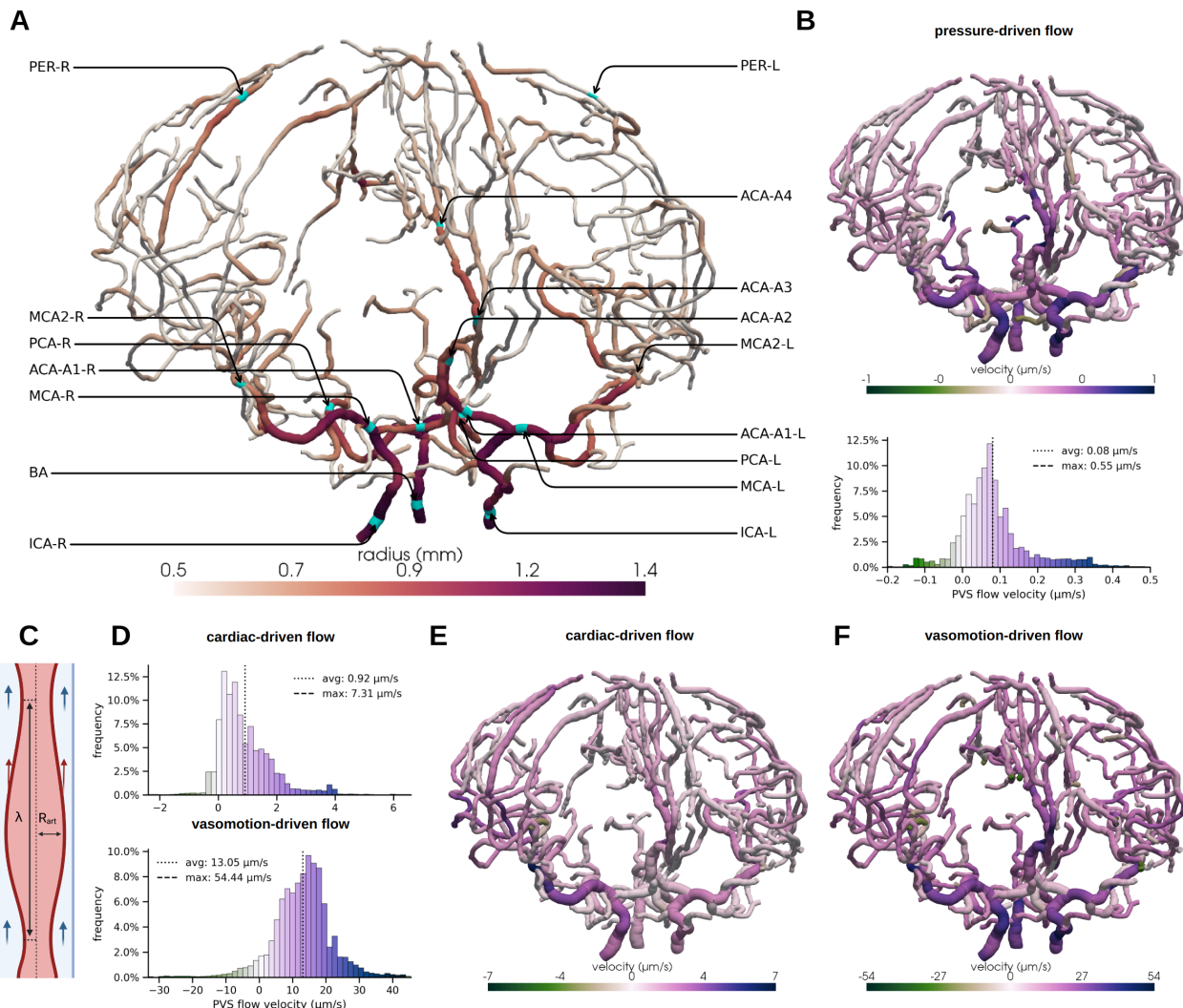


**Figure 3. A static pressure gradient and peristaltic pumping are potential drivers of perivascular flow.** A) Surface arterial network colored by arterial radius with vessel locations labeled; B) Net PVS flow induced by CSF production alone (ef. see also Figure 2—histograms D). Histograms show the relative frequencies of local periarterial velocities. Positive values indicate antegrade PVS flow, while negative values indicate retrograde PVS flow; C) Illustration of the concept of peristaltic pumping; D) histograms of estimated net PVS flow induced by pulse wave or vasomotion peristaltic pumping; E) Estimated net PVS flow induced by pulse wave peristaltic pumping alone. F) Estimated net PVS flow induced by vasomotion/slow wave peristaltic pumping alone.

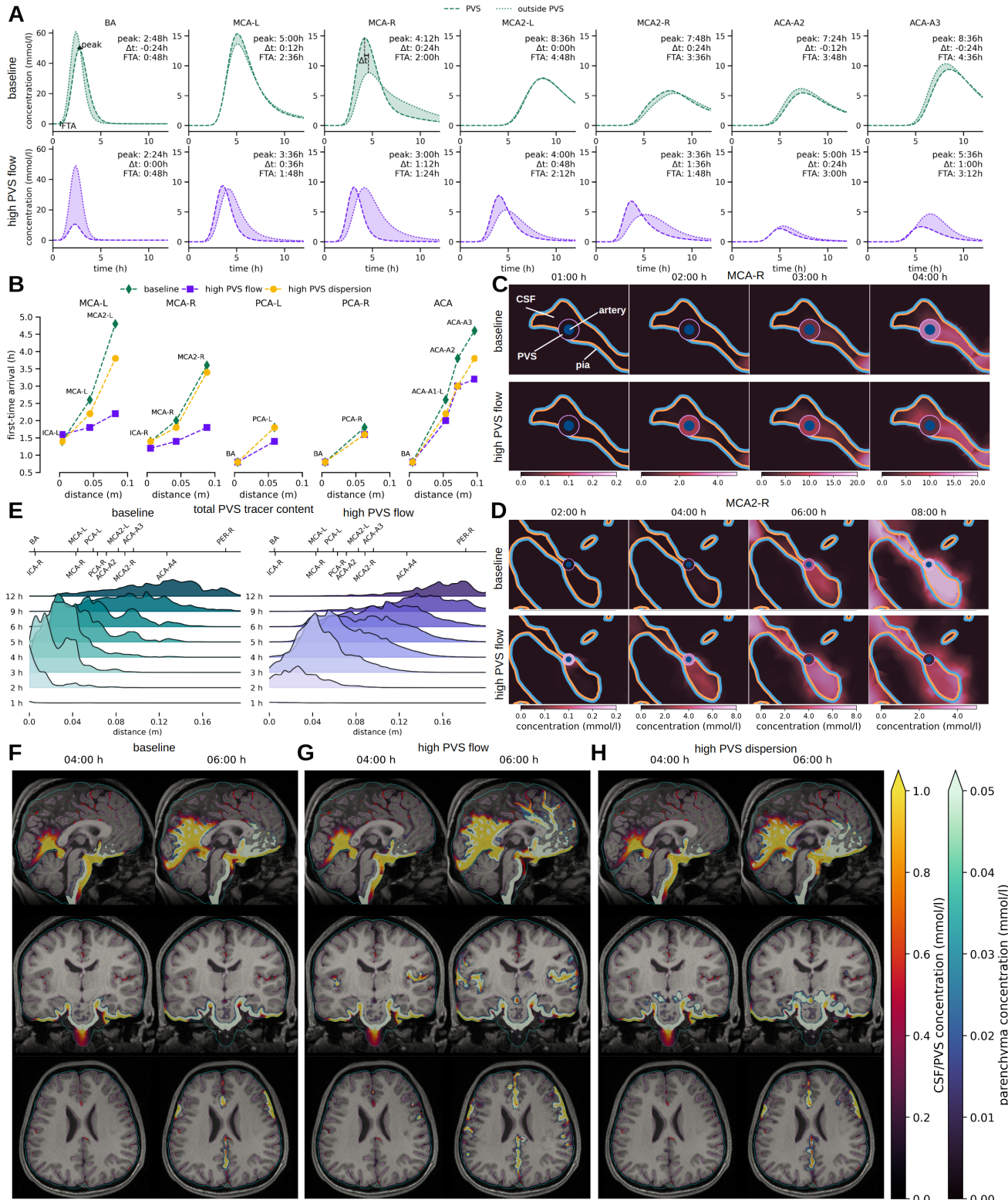


**Figure 4. Perivascular flow shapes and accelerates molecular enrichment. Perivascular flow shapes and accelerates molecular transport.** A) Comparison of mean tracer concentration in the PVS and over the outer PVS surface at key locations of the arterial tree, for the baseline (lower) and high PVS flow (upper) models, with labels: “peak”: time-to-peak (h), “ $\Delta t$ ”: time difference between peaks (h), and “FTA”: first-time tracer arrival (h). B) first-time arrival for the main trunks of the periarterial network over the distance from the closest network root node (BA, ICA-R or ICA-L for the baseline, the high PVS flow and the high PVS dispersion models);

**Figure 4. (cont.)** C, D) 2D slices showing zoom-in on the region surrounding the MCA-R and MCA2-R for the baseline (upper) and high PVS flow (lower) models. Innermost circle indicates the artery (blue), the surrounding annulus is the PVS (color represents concentration value), the surroundings are parenchyma and/or CSF spaces, separated by the pia (blue: towards the parenchyma, pink: towards the CSF); E) Total amount of tracer in the periarterial spaces as a function of the distance to the nearest network root over time for the baseline (left) and the high PVS flow (right) models; F–H) sagittal (upper) and coronal (lower) views of the simulated tracer concentrations overlayed on the T1-weighted MR image after 4 and 6h for the baseline (K), high PVS (L) and high PVS dispersion (M) models (concentration opacity linearly increasing with concentration value, pial surface outlined in pink, arachnoid membrane in cyan, and arteries in dark red). An interactive visualization of the baseline and the high PVS flow model can be found [here](#), and [here](#).

187 Summarizing and quantifying these observations (Figure 5F), we find that neither the time of first arrival nor the time-to-peak  
 188 are substantially affected by the PVS-CSF permeability at any of the periarterial segments considered (BA, MCAs, ACAs).  
 189 However, the concentration difference between the PVS and its surrounding CSF quickly decreases with higher permeability,  
 190 as does the time lag between the concentration peaks in these domains. Thus, fast transport along the PVS is not contingent  
 191 upon a structural compartmentalization of the PVS, whereas a sharp concentration gradient between PVS and CSF is unlikely  
 192 without a restricting barrier.

### 193 Enlarged PVSs in the SAS delay periarterial and intracranial molecular tracer enrichment

194 ~~Enlarged PVSs are associated with impaired periarterial tracer transport and more generally with cognitive decline as well as~~  
 195 ~~certain subtypes of dementia~~<sup>29,93</sup> ~~Idiopathic normal pressure hydrocephalus (iNPH), a dementia subtype, is associated with~~  
 196 ~~enlarged PVS in the SAS and impaired periarterial and parenchymal tracer transport~~<sup>29</sup>. More generally, enlarged PVSs are  
 197 ~~associated with a range of pathophysiological conditions and cognitive decline~~<sup>93</sup>. A key question is thus whether enlarged PVSs  
 198 alone leads to delayed perivascular and intracranial tracer enrichment. To address this question from a fluid and transport  
 199 dynamics perspective, we ask our in-silico model to predict the integrated effect of perivascular dilation on PVS flow velocities  
 200 and tracer enrichment patterns (Figure 6A).

201 Again we compute CSF production-, cardiac-, and vasomotion-induced net PVS flow velocities, but now in a perivascular  
 202 geometry with an increased outer radius ( $R_2^{\text{dilated}} = 3R_1$ ) compared to the previous ( $R_2^{\text{control}} = 2R_1$ ), which corresponds to a  $2.67 \times$   
 203 increase in PVS cross-section area. The enlargement yields notable and non-uniform changes in the flow dynamics. On the one  
 204 hand, the pressure-induced flow velocities increase from a mean of  $0.08 \mu\text{m/s}$  to  $0.33 \mu\text{m/s}$  due to the reduced effective resistance  
 205 of the PVS. However, the peristaltic pumping becomes considerably less effective: the cardiac and vasomotion-induced net CSF  
 206 flow velocities drop from a mean of  $0.92 \mu\text{m/s}$  to  $0.17 \mu\text{m/s}$  and from  $13.05 \mu\text{m/s}$  to  $2.33 \mu\text{m/s}$ , respectively (Figure 6B–D). In  
 207 total, the net CSF velocity reduces, which in turn alters the tracer enrichment within the dilated PVS. Notably, we observe later  
 208 tracer arrival in all MCA segments, with up to 96 min later arrival in the MCA2s for the high PVS flow scenario (Figure 6E,  
 209 F). For the baseline model, which omits the vasomotion-induced net PVS flow, the effect is less pronounced in the MCA but  
 210 clearly persists and is evident in the MCA2s (Figure 6F). Finally, we note that the larger volume of the dilated PVS results in  
 211 a greater total accumulation of tracer in the PVS from 3–24 hours and reduced enrichment of the parenchyma at 6 and 12 h,  
 212 while the mean PVS concentration is initially lower, but later exceeds the baseline model (Figure 6G,H).

## 213 Discussion

214 We have presented a high-fidelity in-silico model of molecular enrichment transport and clearance in human intracranial spaces,  
 215 enabling tailored predictions of the influence of CSF space and (peri)vascular morphology, physiological factors such as cardiac  
 216 and respiratory pulsatility, as well as of pathological conditions such as enlarged PVSs in the SAS. A key observation is that  
 217 the balance between CSF production and intracranial pulsatility significantly shapes the large-scale features of molecular tracer  
 218 enrichment, with e.g. ventricular tracer reflux after intrathecal injection in the absence of CSF production, and preference  
 219 towards anterior brain regions with reduced pulsatility. Indeed, the simulated distribution patterns cover a substantial range of  
 220 the individual variations observed clinically<sup>15</sup>. In terms of perivascular pathways, we find that even moderate CSF flow on  
 221 the order of  $0.1\text{--}1.0 \mu\text{m/s}$  in the surface PVSs results in earlier tracer enrichment around major cerebral arteries. This effect  
 222 is more pronounced – with up to a three-hour difference in time of arrival – with mean PVS flow rates of approximately  $10 \mu\text{m/s}$ . Our models of CSF flow in perivascular networks, based on first principles and asymptotic analysis, predict net flow of  
 223 such magnitudes and both antegrade and retrograde flow within the perivascular network, occurring with or without pressure  
 224 differences at the network ends. The PVS may thus function as highways facilitating rapid transport, even in the absence of  
 225 structural barriers, though a sharp concentration difference between the PVS and surrounding tissues is unlikely without such  
 226 barriers. Finally, dilated PVS in the SAS will cause a substantial reduction in cardiac- and vasomotion-driven flow velocities,  
 227

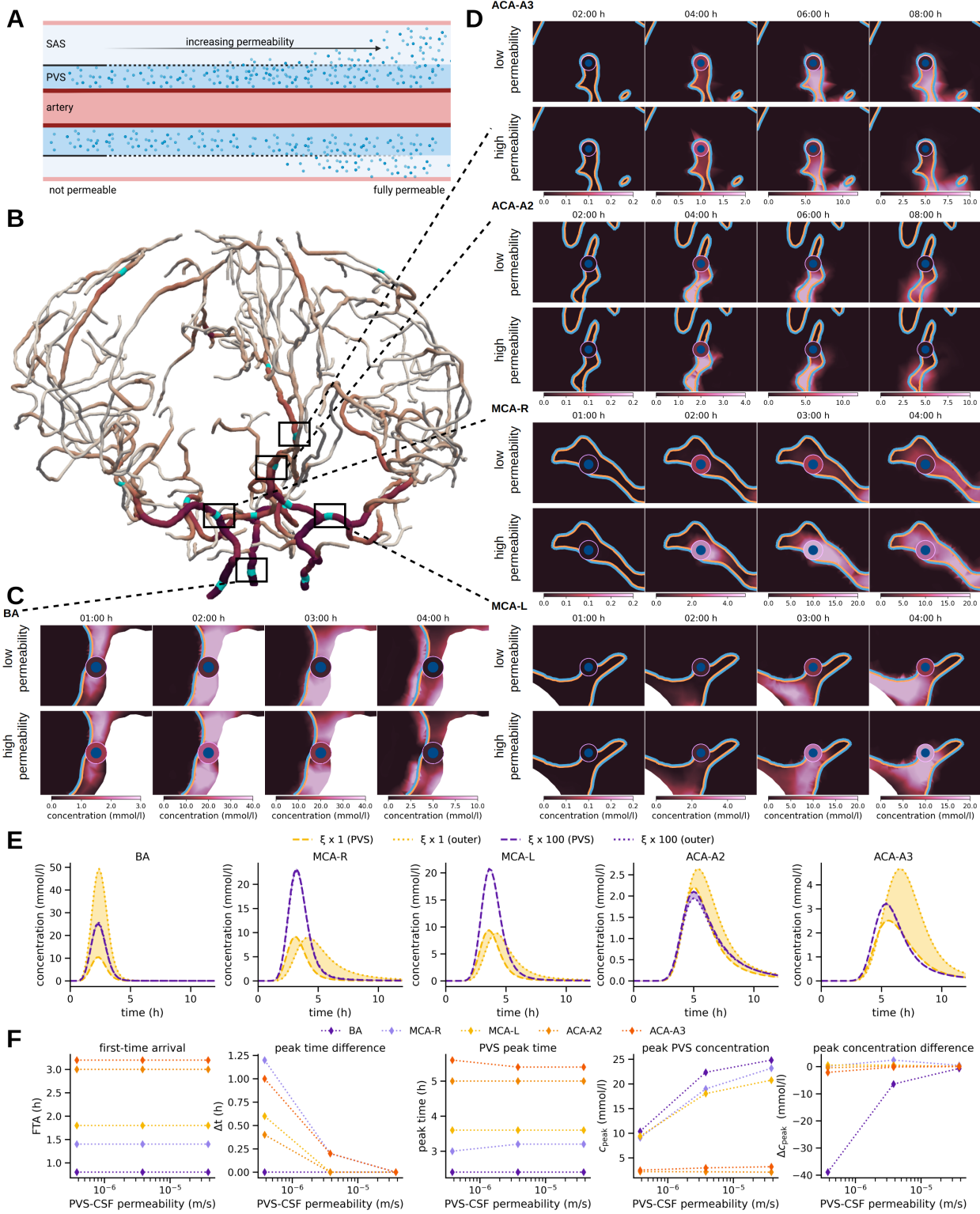


**Figure 5. Does early perivascular enrichment rely on a structural compartmentalization of the PVS?** A) The PVS-CSF membrane permeability regulates the exchange of solutes between the PVS and surrounding CSF spaces; B) The arterial network with highlighted regions of interest; C) 2D slices showing zoom-in to the region surrounding the basal artery after 1, 2, 3, and 4 hours for a low (above) and high (below) PVS-CSF permeability model. Innermost circle indicates the artery (blue), the surrounding annulus is the PVS (color represents concentration value), the surroundings are parenchyma and/or CSF spaces, separated by the pia (blue: towards the parenchyma, pink: towards the CSF). The cutting planes are normal to the blood vessels; D) As in (C) for regions surrounding (from upper to lower) the ACA-A3, ACA-A2, MCA-R and MCA-L segments;

**Figure 5. (cont.)** E) Comparison of mean tracer concentration in the PVS (dashed) and over the outer PVS surface (dotted) for the BA, MCA-R, MCA-L, ACA-2, and ACA3 segments over time for the high (purple) and low permeability (yellow) models; F) Effect of varying the PVS-CSF permeability on first-time-of-arrival (FTA), time difference ( $\Delta t$ ) between concentration peaks in the PVS and surrounding tissue, time of PVS peak concentration, PVS peak concentration and difference in peak concentration between PVS and surrounding tissue.

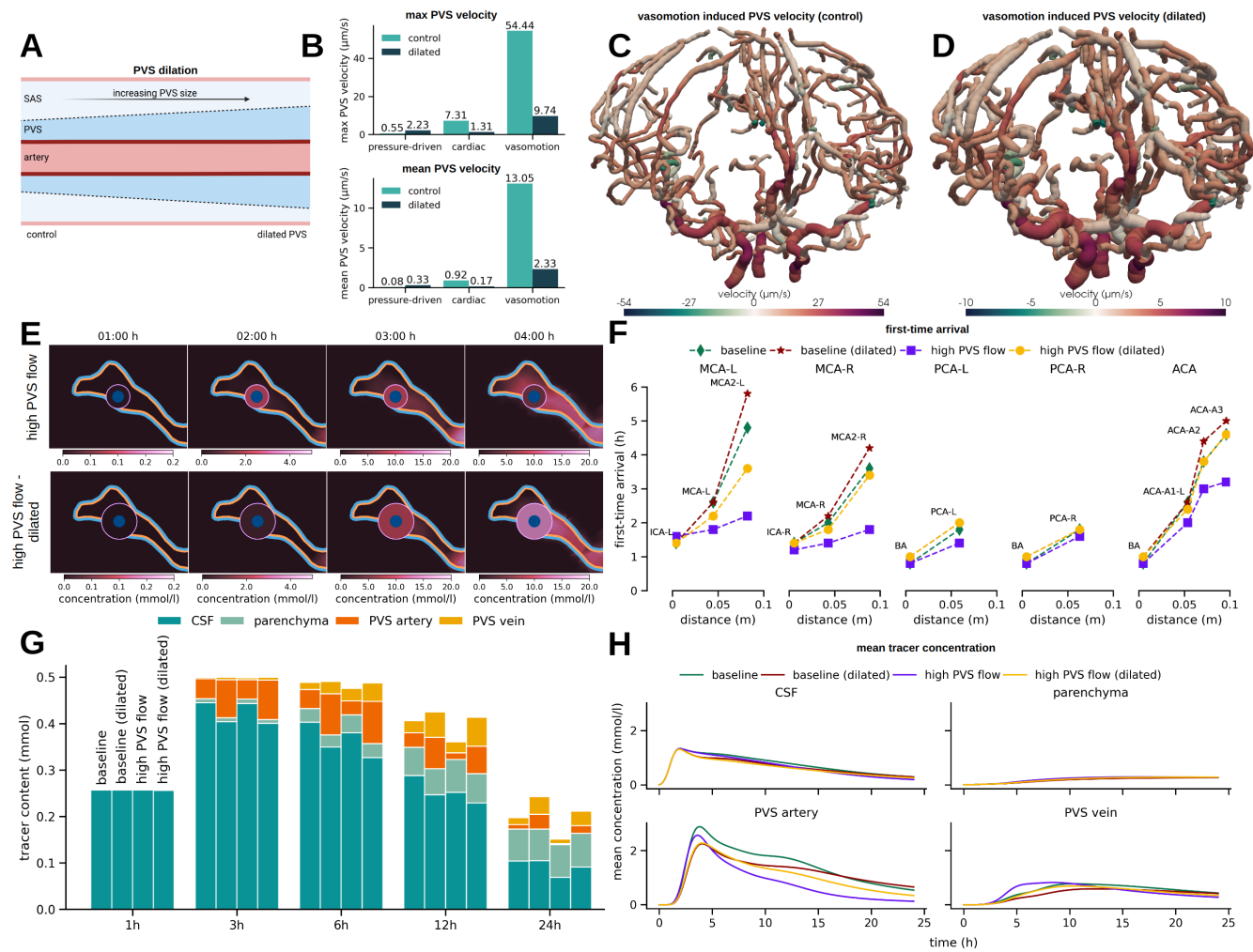


**Figure 6. PVS enlargement reduces net PVS flow and delays tracer transport** A) Modelling dilated PVS in the SAS by extending the outer PVS boundaries; B) mean and max PVS flow velocities with normal/control and dilated PVS; C-D) 3D rendering of vasomotion-induced PVS flow in the normal (C) and dilated (D) periarterial networks; E) 2D slices showing zoom-in to the region surrounding the MCA-R after 1, 2, 3, and 4 h with normal (lower) and dilated (upper) PVS. Innermost circle indicates the artery (blue), the surrounding annulus is the PVS (color represents concentration value), the surroundings are parenchyma and/or CSF spaces, separated by the pia (blue: towards the parenchyma, pink: towards the CSF). The cutting plane is normal to the blood vessel; F) First-time arrival for different branches of the arterial tree for the baseline model (with pressure-driven and cardiac-induced net PVS flow) and the high PVS flow model (also including vasomotion-induced net PVS flow) for normal and dilated PVS; G) total tracer content in the CSF, parenchyma and arterial and venous PVS at 1,3,6,12 and 24 h for the four models from F; H) mean concentration in the CSF, parenchyma and arterial and venous PVS over time for the four models from F.

which in turn impedes perivascular transport.

While ~~molecular tracer~~ enrichment of the brain and surrounding CSF spaces have been extensively studied in animal models, especially in murine models in connection with studies of the glymphatic system, there are fewer reports of contrast enrichment in human subjects over 0–24h. We therefore mainly compare our in-silico predictions with the series of papers by Eide and colleagues<sup>6,11,15,29</sup> and Watts et al<sup>68</sup>. Ringstad et al.<sup>15</sup> report of tracer enrichment in a centripetal pattern, primarily in regions near large cerebral surface arteries, peaking in the CSF spaces between 6 and 9 hours, with parenchymal tracer content still increasing after 24 hours, but with large individual differences. Watts et al<sup>68</sup> report of a similar enrichment pattern and a concentration peak in the SAS of  $\approx 0.5$  mmol/l (relative to a total amount of 1.0 mmol) occurring after 10 to 15 hours. Our in-silico enrichment patterns agree with these observations, though with an earlier rather than later peak in the CSF spaces (2 hours after first tracer appearance at the craniocervical junction). In particular, we note that the substantial individual variation observed clinically is comparable to the variation in in-silico enrichment patterns associated with reduced CSF production or reduced intracranial pulsatility. We find that about 20% of the tracer reaching the cranium enters the parenchyma, which aligns with the reported peak concentration values of 0.5 mmol/l in the SAS and 0.1 mmol/l in the parenchyma reported by Watts et al<sup>68</sup>. ~~In terms of perivascular tracer enrichment, Eide and Ringstad<sup>29</sup> report of first-time tracer appearance~~

~~Importantly, our simulation results indicate that the tracer enrichment observed clinically relies on the presence of one or more flow drivers in addition to CSF production and cardiac peristalsis. Dispersion due to cardiac and respiratory pulsations has been hypothesized to enhance transport in the perivascular spaces as well as in the CSF spaces. However, recent estimates indicate that the effect of dispersion in the PVS of the MCA after  $37.8 \pm 47.0$  (M1),  $53.1 \pm 50.5$  (M2) and  $82.6 \pm 61.5$  (M3) min after injection, thus with just a~~ does not exceed a factor of 2 compared to diffusion alone<sup>43,44,47,87</sup>. Our model demonstrates that not even a 100-fold increase in the PVS dispersion coefficient accelerates transport substantially (Figure 4 H). To illustrate the need for a stronger advective driver, we compared our findings to tracer arrival times reported by Eide and Ringstad<sup>29</sup>, who observed a delay of just 15.3 min ~~delay between M2 and between the M1~~. Comparing with our FTAs in the MCA segments and M2 segments of the MCA. First, we note that the ~~baseline model predicts a more than 3 hour difference in FTA between the M1 and M2 spaces studied by Eide and Ringstad<sup>29</sup>, labeled therein as the PVSAS, are naturally compared to the parts of our surface PVS networks embedded within the SAS. Our baseline model, accounting only for CSF production and cardiac-driven flow, predicted a physiologically unrealistic delay of over three hours. In contrast, the our high PVS flow scenario predicts a~~, which incorporates the effects of low-frequency vasomotion, yielded a more consistent delay of 24 min ~~delay between these segments. Moreover, the high PVS flow scenario predicts FTAs of 84–108 min (M1) and 108–132 min (M2) after tracer appearance at the craniocervical junction. Assuming a tracer minutes. Furthermore, after adjusting for the 13 min travel time from the point of injection to the craniocervical junction of 13 min (as reported by Eide and Ringstad<sup>29</sup>), our predictions fall at~~<sup>29</sup>, the high PVS flow model's FTAs (84–108 min for M1) aligns well with the upper end of the ~~clinical ranges. This can partly be attributed reported clinical range ( $37.8 \pm 47.0$ ), particularly when considering potentially delayed transport due to the limited caudal extend extent of our PVS network, with the lowest point located approximately 4 cm above the craniocervical junction due to imaging constraints. We~~. All in all, we interpret these results as ~~indicative of a net CSF flow in human surface PVS beyond what would be induced~~ strongly indicative of that PVS flow driven by CSF production and cardiac peristalsis alone ~~is insufficient to explain the rapid perivascular transport observed in humans~~.

The existence, magnitude, and directionality of flow in surface and parenchymal PVSs have been the subject of active debate for decades<sup>10,14,22,25,31–35,37–42,45,48,85,94</sup>. In mice, Mestre et al<sup>34</sup> observe CSF flow in surface perivascular regions surrounding branches of the MCA with average flow speeds of 18.7  $\mu\text{m}/\text{s}$  and net flow in the antegrade direction, but also regions with retrograde flow. Similarly, Bedussi et al.<sup>33</sup> report of oscillatory flow, with an average (net) CSF velocity of  $17 \pm 2$   $\mu\text{m}/\text{s}$  in the antegrade direction. Using physics-informed neural networks, Boster et al<sup>35</sup> estimate PVS velocities of  $12.75 \pm 6.25$   $\mu\text{m}/\text{s}$ . Less is known about the magnitude and directionality of CSF flow in surface PVSs in humans. Here, assuming that human surface PVS follow the major surface vessels and are CSF-filled but otherwise open regions of width proportional to the vessel radius, our estimates indicate that the CSF pressure differences due to CSF production, cardiac peristaltic pumping and low-frequency vasomotion all yield spatially-varying net CSF flow with both antegrade and retrograde PVS segments. This observation is thus in agreement with the experimental observations<sup>33,34</sup>, and inherently supports the original notion that antegrade and retrograde solute transport along PVSs may coexist<sup>22</sup>. In terms of magnitude, the contribution from CSF production and cardiac wall motion are small (0.08  $\mu\text{m}/\text{s}$  and 0.92  $\mu\text{m}/\text{s}$  on average), but intriguingly, our estimates of the contribution from vasomotion (13.05  $\mu\text{m}/\text{s}$ ) are comparable to the experimental reports. We do note that this estimate is based on the presence of rhythmic waves of vasomotion at a frequency of 0.1Hz, a wavelength of 20 mm, and a wall displacement of 10% – in the antegrade direction, all values currently associated with ~~significant uncertainty~~<sup>85,88,95</sup> ~~major uncertainty~~<sup>85,86,88,95</sup>. In particular, Broggini et al<sup>88</sup> report of near-0.1Hz vasomotion waves traveling both antegrade and retrograde along pial arterioles in mice, while Munting et al<sup>86</sup> report of vessel diameter changes at similar frequencies mainly (but not entirely) in the retrograde direction. To the best of our knowledge, less is known about vasomotion wave characteristics in the human cerebral vasculature, though Gokina et al<sup>95</sup> report of spontaneous vasomotion also in human pial arteries ex-vivo.

To what extent are surface PVSs in communication with the surrounding SAS and to what extent are these structurally separated compartments? Originally, Weller and coauthors<sup>23,60,91</sup> identified thin sheaths of pial cells surrounding human surface arteries and penetrating arterioles (but not veins or venules). On the other hand, Bakker and coauthors report that the subarachnoid space, the cisterns, ventricles and penetrating periarteriolar spaces form a continuous CSF space<sup>61</sup>. Thorne and colleagues study the architectures of rat perivascular spaces in detail, emphasizing the presence of openings (stomata) on the interface between the vasculature and the CSF within the SAS<sup>27,62</sup>. Further, Mestre et al<sup>63</sup> study the properties of pial perivascular spaces in mice, and report of pial cells forming sheaths for larger surface arteries and partially cover smaller surface arteries, with higher coverage in ventral SAS regions. Our results demonstrate that the PVSs may act as rapid transport pathways even with only a partial barrier between the PVS and surrounding CSF, thus contributing to quantifying the properties of the human PVS-CSF interface<sup>29</sup>. In this regard, we emphasize that we report on the isolated effect of variations in permeability on molecular transport, separated from any effects on fluid flow in the PVS. Clearly, one may expect that the presence and/or properties of such a barrier would affect also PVS flow. However, considering the uncertainty associated with PVS flow characteristics in the human SAS in general and the lack of computational models describing net PVS flow in the presence of fluid exchange, this remains challenging to quantify.

Lifestyle factors such as sleep<sup>5,6,8,9,87,96,97</sup>, exercise<sup>98,99</sup>, and alcohol intake<sup>100</sup> affect molecular enrichment transport and clearance of the brain. In particular, pial arteries display higher-amplitude low-frequency vasomotion during NREM and intermediate sleep states, while REM sleep is associated with reduced PVS width<sup>87</sup>. Peristaltic pumping is more effective under both of these configurations, resulting in higher estimated net PVS flow velocities<sup>41</sup>. Even higher PVS velocities would amplify the PVS flow effects simulated here, with earlier arrival times along the PVSs, clear enrichment in adjacent spaces, and accelerated molecular tracer enrichment overall. Moreover, sleep is linked with low-frequency oscillations in human CSF flow<sup>55</sup>. As we have shown here, the level of dispersion in the CSF spaces strongly shapes molecular enrichment transport patterns. While we, at baseline, account for the dispersion induced by cardiac and respiratory pulsatility, the high dispersion scenarios considered can be viewed as representative of additional pulsatility induced by e.g. neural waves<sup>55,58</sup> or other respiration patterns depending on activity level. More broadly, we consider this as a key strength of the current in-silico framework: allowing for integrating and exploring the mechanistic macroscale implications of changes in pulsatility at smaller spatial or temporal scales. This approach of modeling pulsatility through an effective dispersion factor is a simplification that does not capture the full complexity of transient fluid dynamics, such as non-uniform wall motion and ependymal cilia within the ventricular system<sup>101</sup>, dynamic CSF flow at the craniocervical junction, or the effect of microanatomical features such as subarachnoid trabeculae on flow resistance and dispersion in the SAS. However, our approach is supported by recent clinical observations. High-resolution MRI measurements by Hirschler et al.<sup>36</sup> revealed that CSF mobility in regions with high pulsatility is approximately tenfold greater than the self-diffusion of water, an enhancement factor consistent with the values computed in our model.

In terms of limitations, our primary constraint modelling-wise is the geometric representation of the vascular (and therefore also perivascular) networks. Concretely, we account for no vessels below the original MRI resolution limits, and thus only a part of the cerebral surface vasculature and effectively not the cortical vessels. In addition, and again due to lack of resolution, there is uncertainty associated with the location of the vessel segments relative to the CSF spaces and parenchyma, with some vessels surrounded by both domains and some vessels completely entering the parenchyma before returning to the SAS. Higher resolution MRI data (T1w and e.g. time-of-flight, QSM or other modalities) in more subjects would immediately allow for more detailed studies of this aspect. As a result of the lack of an accurate representation of the cortical and subcortical white matter vasculature, we have considered a conservative basic transport model within the parenchyma, modelling extracellular diffusion alone and no bulk interstitial fluid flow. To compensate, we have focused on reporting detailed predictions in the CSF spaces and surface PVS after not more than 24 hours. In particular, we note that, we observe tracer accumulation at the perivascular network ends after 12 hours, similar to that previously observed for microspheres<sup>33,34</sup>, which here can be interpreted as an artifact of the incomplete network creating up a barrier for tracer movement. Previously, by inferring transport parameters within the human brain from glymphatic MRI data, we have found that enrichment molecular transport within the parenchyma is well-represented by  $\approx 3\times$  enhanced diffusion augmented by local clearance e.g. across the blood-brain barrier or, or by diffusion-convection with a complex pattern of spatially-varying convective velocities interstitial fluid flow on the order of  $1\text{-}10 \mu\text{m}/\text{min}$ <sup>96</sup>. We will incorporate such transport mechanisms within the parenchyma in future work. Finally, we also note that we simulate the intracranial distribution of a tracer concentration appearing at the craniocervical junction rather than as an intrathecal injection. We thus neglect absorption of both CSF and tracer in the spinal compartment, and therefore overestimate the amount of tracer entering into the intracranial spaces; however, due to the linearity of the mathematical model, it is valid to directly interpret the in-silico concentrations relative to the total amount of tracer.

In conclusion, our findings transfer insights from experimental studies and theoretical analysis to the in-silico human setting, reconcile seemingly conflicting observations in particular relating to directionality of perivascular flow, and integrate different physical mechanisms across across spatial and temporal scales. The complete simulation pipeline is openly available,

338 including interactive visualization of simulation results for all model variations<sup>69</sup>. Future work will focus on further model  
 339 validation including comparisons between in-silico predictions and glymphatic MRI for a number of subjects across several  
 340 patient cohorts. Looking ahead, this platform establishes a foundation for in-silico studies of molecular movement within the  
 341 human brain environment, such as tailored predictions of intrathecal chemotherapy delivery or personalized diagnostics of  
 342 brain clearance capacity.

## 343 Methods

344 This section gives a condensed summary of the in-silico modelling framework. For a complete description of the mathematical  
 345 models and simulation scenarios, we refer to the Supplementary information S1.

### 346 Intracranial compartments: ventricular system, SAS, and brain parenchyma

347 From T1-weighted MR images of a 26-year-old, healthy male volunteer<sup>67</sup>, we first automatically segment the brain parenchyma  
 348 and CSF spaces, including the ventricular system and SAS, using Synthseg<sup>102,103</sup> (Figure 1A–B). We next manually adjust the  
 349 segmentation to accurately represent the connections and barriers between CSF spaces (aqueduct, median aperture, tentorium  
 350 cerebelli), smoothen, and finally extract surface representations of the outer (arachnoid) boundary, the pial membrane and  
 351 other interfaces. Conforming to these surface and interface representations, we generate a tetrahedral mesh  $\Omega$  representing the  
 352 complete intracranial volume as the union of the parenchyma  $\Omega_{\text{PAR}}$  and CSF spaces  $\Omega_{\text{CSF}}$ , using fTetWild<sup>104</sup> (Figure 2A–B).  
 353 The resulting computational mesh consists of 233 592 vertices and 1 290 131 mesh cells, which vary between 0.22 mm and 8.9  
 354 mm in mesh cell diameter. The parenchyma has a total volume of 1318 ml, whereas the ventricles and the outer SAS contribute  
 355 32 ml and 329 ml, respectively, to a total CSF volume of 361ml, in agreement with recent estimates<sup>105</sup>.

### 356 Periarterial and perivenous spaces

357 To represent surface networks of periarterial and perivenous spaces, we use Kiminaro<sup>106</sup> to separately skeletonize time-of-flight  
 358 angiography (ToF) and quantitative susceptibility mapping (QSM) images from the same human subject<sup>67</sup>. This technique  
 359 yields networks of one-dimensional curves, each curve  $\Lambda^i$  indicating the centerline of a blood vessel segment and labeled  
 360 with its lumen radius  $R_1^i$  (Figure 3A). We also assign an outer radius  $R_2^i > R_1^i$  to each segment  $i$ , form the annular cylinder  
 361 ensheathing  $\Lambda^i$  and define the union of these as the PVS. The periarterial network graph consists of 12 708 edges connected at  
 362 12 562 inner nodes and with 147 end nodes, and the associated domain is denoted by  $\Lambda_a$ . We identify three of the end nodes –  
 363 corresponding to the two internal carotid arteries (ICAs) and the basilar artery (BA) – as root nodes, and designate the other  
 364 ends as leaf nodes. The resulting perivenous network graph consists of 24 829 edges connected at 23 881 inner nodes and with  
 365 949 end nodes, and the associated domain is denoted by  $\Lambda_v$ . Finally, we label the outer surface of the PVSs associated with  $\Lambda_a$   
 366 and  $\Lambda_v$ , by  $\Gamma_a$  and  $\Gamma_v$  respectively.

### 367 Molecular transport equations Steady flow in the CSF spaces induced by CSF production

We model diffusion, convection, and exchange of a molecular solute in the PVS networks  $\Lambda_a$  and  $\Lambda_v$ , in the CSF spaces  $\Omega_{\text{CSF}}$  and in the brain parenchyma  $\Omega_{\text{PAR}}$  via a mixed-dimensional transport model<sup>66,107</sup> over a timescale of minutes to hours (Figure 1A–B, Figure 2A–C). Specifically, for  $t > 0$ , we solve for a concentration  $c = c(x, t)$  in the 3D intracranial compartments ( $x \in \Omega_{\text{CSF}}, x \in \Omega_{\text{PAR}}$ ) and for a cross-section averaged concentration  $\hat{c} = \hat{c}(s, t)$  in the periarterial and perivenous networks ( $s \in \Lambda_a, s \in \Lambda_v$ ) such that the following equations hold:

$$\begin{aligned} 2\partial_t(\phi c) - \nabla \cdot (D\nabla(\phi c)) + \nabla \cdot (\mathbf{u}c) + \xi(\bar{c} - \hat{c})\delta_\Gamma &= 0 && \text{in } \Omega_{\text{CSF}}, \Omega_{\text{PAR}}, \\ \partial_t(A\hat{c}) - \partial_s(\hat{D}A\partial_s(\hat{c})) + \partial_s(A\hat{\mathbf{u}}\hat{c}) + \xi P(\hat{c} - \bar{c}) &= 0 && \text{in } \Lambda_a, \Lambda_v. \end{aligned}$$

In ,  $0 < \phi \ll 1$  is the fluid volume fraction,  $D$  and  $\hat{D}$  are effective diffusion coefficients, and  $\mathbf{u}$  and  $\hat{\mathbf{u}}$  are fluid (CSF/ISF)  
 velocities, all defined in the respective compartments;  $P = 2\pi R_2$  is the perimeter and  $A = \pi(R_2^2 - R_1^2)$  the area of the PVS  
 cross-sections,  $\delta_\Gamma$  is a Dirac term concentrated on the interfaces  $\Gamma_a, \Gamma_v$ , the overlined  $\bar{c}$  denotes the average of  $c$  over  
 cross-sections of  $\Gamma_a, \Gamma_v$ , and  $\xi$  is a permeability allowing for transfer/exchange over the interfaces  $\Gamma_a, \Gamma_v$  between the periarterial  
 and perivenous networks and their surroundings. Moreover, we model the membrane between the parenchyma and the CSF  
 spaces as a semi-permeable membrane with permeability coefficient  $\beta_{\text{pia}}$ . For a complete description of this mathematical  
 model and simulation scenarios, see the Supplementary information S1. The initial concentrations in the three-dimensional  
 domain  $\Omega$  and networks  $\Lambda_a, \Lambda_v$  are all set to zero.

### 376 **Intracranial influx after intrathecal injection**

To represent molecular influx into the intracranial compartments following intrathecal injection, without modelling the spinal compartment explicitly, we prescribe a time-dependent molecular influx over the interface towards the spinal CSF compartment with the condition:

$$(D \nabla c - \mathbf{u}c) \cdot \mathbf{n} = g_{\text{influx}}, \quad \text{on } \Gamma_{\text{SSAS}}.$$

Here we set

$$g_{\text{influx}}(t) = \frac{m_{\text{tot}}}{T_{\text{max}}^2 |\Gamma_{\text{SSAS}}|} \max(0, T_{\text{max}} - |t - T_{\text{max}}|),$$

377 which expresses a hat-shaped influx function with a peak at  $T_{\text{max}}$  and a total tracer injection of  $m_{\text{tot}}$  (Table 1).

### 378 **Molecular clearance from the intracranial space and perivascular network ends**

379 We model molecular clearance, into the meningeal lymphatics or other pathways, across the upper, outer (arachnoid) boundary  
380 (Figure 1A, Figure 2C), proportional to the concentration in the SAS with a rate constant  $\beta_{\text{exit}}$ . We set a no-flux condition at  
381 the end nodes of the perivascular networks, not allowing for direct molecular clearance there.

### 382 **CSF flow in the SAS and ventricular system**

383 We model CSF as an incompressible Newtonian fluid at low Reynolds and Womersley numbers via the Stokes equations  
384 with viscosity  $\mu$ , and account for the convective contribution of the (see Table 1 for parameter values). To account for steady  
385 flow induced by CSF production in the choroid plexus. Specifically, we compute the velocity CSF velocity field  $\mathbf{u}_{\text{CSF}}$  and  
386 associated pressure field  $p_{\text{CSF}}$  in the SAS and ventricular system induced by a constant  $\Omega_{\text{CSF}}$  that result from a steady CSF  
387 production at a rate of  $u_{\text{in}}$  across the lateral ventricle walls and with (Figure 2A–E). We allow for CSF efflux across the upper,  
388 outer (arachnoid) boundary with efflux resistance  $R_0$ , and then set  $\mathbf{u} = \mathbf{u}_{\text{CSF}}$  in  $\Omega_{\text{CSF}}$  in (Table 1, Figure 2A–E, see also the  
389 Supplementary information ( $R_{\text{CSF},0}$ ).

### 390 **Perivascular fluid flow induced by CSF production**

391 To estimate the contribution also to perivascular fluid flow from CSF production, we impose the fluid pressure  $p_{\text{CSF}}$  induced  
392 by CSF production, computed in the SAS and ventricular system, at the end nodes of the periarterial network. For the end  
393 nodes located within the SAS ( $v \in \Omega_{\text{CSF}}$ ), the value  $p_{\text{CSF}}(v)$  is used directly, while for the end nodes located within the  
394 parenchyma ( $v \in \Omega_{\text{PAR}}$ ), we compute and apply a harmonic extension  $E(p_{\text{CSF}})(v)$ . We then numerically solve a system of  
395 hydraulic network equations to compute  $\hat{u}_a^p$  defined over  $\Lambda_a$ ; i.e., the CSF production-induced velocity field in the periarterial  
396 network. We refer to Supplementary information S1)). We do not model bulk flow within the brain parenchyma, except  
397 within the perivascular network segments extending below the pial surface, and thus set  $\mathbf{u} = 0$  in  $\Omega_{\text{PAR}}$  in .1.4 Steady flow  
398 in perivascular networks induced by pressure differences for details. We repeat this procedure to compute a corresponding  
399 velocity field  $\hat{u}_v^p$  in the perivenous network  $\Lambda_v$ .

### 400 **Dispersion in the CSF spaces induced by pulsatile CSF flow**

401 The pulsatile flow of CSF in the SAS and ventricular system, associated with the cardiac and respiratory cycles, substantially  
402 enhances molecular diffusion through dispersion<sup>43, 44, 47, 78, 108, 109</sup>. To account for these dispersive effects, while bridging  
403 from the pulsatile flow time scale of seconds to a molecular transport time scale of hours, we compute cardiac estimate  
404 cardiac- and respiratory dispersion factors ( $R_c$  and  $R_r$ , both spatially-varying,) in  $\Omega_{\text{CSF}}$  (Figure 2A) by combining G, I). To  
405 compute these spatially-varying factors, we rely on a simplified model that combines computational estimates of the respective  
406 peak CSF pressure gradients (Figure 2F, H) with theoretical estimates for shear-augmented (Taylor) dispersion<sup>44, 108, 109</sup> (see  
407 Supplementary information S1.3 *Estimating dispersion factors from pulsatile CSF flow* for a complete description). Combining  
408 these the cardiac and respiratory effects, we then set  $R = R_c + R_r$  and define the effective diffusion coefficient  $D = (1+R)D^{\text{Gad}}$   
409 in  $\Omega_{\text{CSF}}$  in the baseline model.

### 410 **Perivascular fluid flow induced by CSF pressure differences**

411 To estimate the contribution also to perivascular fluid flow from CSF production, we impose the fluid pressure  $p_{\text{CSF}}$  induced  
412 by CSF production, computed in the SAS and ventricular system, at the end nodes of the periarterial network located within  
413 the SAS. For the network end nodes located within the parenchyma, we compute a harmonic extension of the CSF pressure  
414 field (by solving a Laplace equation in  $\Omega_{\text{PAR}}$  with  $p_{\text{CSF}}$  as the boundary value), and set the corresponding value at these  
415 end nodes. We then numerically solve a system of hydraulic network equations to compute  $\hat{u}_a^p$  defined over  $\Lambda_a$ ; i.e., the  
416 pressure-difference induced CSF flow velocity in the periarterial network (see also Supplementary information S1.1.4). We  
417 repeat this procedure to compute a corresponding velocity  $\hat{u}_v^p$  in the perivenous network  $\Lambda_v$ .

## 418 Perivascular fluid flow induced by arterial wall motion

419 Using the theoretical framework introduced by Gjerde et al.<sup>41</sup>, we also compute analytic estimates for the time-average  
 420 perivascular flow rate  $\langle Q' \rangle$  induced by peristalsis in the arterial network  $\Lambda_a$ ; i.e. the net flow induced by traveling waves  
 421 of arterial wall motion of frequency  $f$ , amplitude  $\varepsilon$  and wave lengths  $\lambda$  (Figure 3C). The corresponding contribution to the  
 422 periarterial flow velocity is defined for each segment  $\Lambda_i$  as  $\langle Q'_i \rangle / A_i$  where  $A_i = \pi(R_2^i - R_1^i)$  is the cross-section area of the  
 423 PVS segment and  $\langle Q'_i \rangle$  is the estimated mean flow rate (see Supplementary information S1.4 *Estimating net perivascular*  
 424 *flow induced by peristaltic waves* for more details). Two wall motion patterns are considered, *yielding*  $\hat{u}_a^c$  and  $\hat{u}_a^v$  *respectively*:  
 425 *cardiac pulsations* with  $f = 1.0\text{Hz}$ ,  $\lambda = 2\text{ m}$  and  $\varepsilon = 1\%$  *yielding*  $\hat{u}_a^c$  (Figure 3D), and very low-frequency *vasomotion* with  
 426  $f = 0.1\text{Hz}$ ,  $\lambda = 0.02\text{m}$ , and  $\varepsilon = 10\%$  *yielding*  $\hat{u}_a^v$  (Figure 3E). No flow induced by peristalsis is considered for the perivenous  
 427 network. In the baseline model, we combine the contributions from CSF production and cardiac peristalsis to set  $\hat{u}$  *in*-as  
 428  $\hat{u}_a = \hat{u}_a^P + \hat{u}_a^c$  in  $\Lambda_a$ , and  $\hat{u}_v = \hat{u}_v^P$  in  $\Lambda_v$ . *We remark that none of these models account for fluid exchange across the lateral*  
 429 *outer interface of the PVSs (over  $\Gamma_a, \Gamma_v$ ), while fluid entry and exit is allowed at the end nodes of the PVS networks.*

## 430 Molecular transport equations

431 We represent the evolution and distribution of a solute in the CSF spaces  $\Omega_{\text{CSF}}$ , brain parenchyma  $\Omega_{\text{PAR}}$ , and periarterial and  
 432 perivenous networks  $\Lambda_a \cup \Lambda_v$  via a mixed-dimensional transport model<sup>66</sup> over a timescale of minutes to hours (Figure 1A–B,  
 433 Figure 2A–C). The current model accounts for solute exchange between the CSF spaces, brain parenchyma, and the PVSs,  
 434 diffusion within all compartments, dispersion and convection in the CSF spaces, and convection within the PVS. Specifically,  
 435 for  $t > 0$ , we solve for a concentration field  $c(x, t)$  in the 3D intracranial compartments (for  $x \in \Omega_{\text{CSF}} \cup \Omega_{\text{PAR}}$ ) and for a cross  
 436 section-averaged concentration field  $\hat{c}(s, t)$  in the perivascular networks (for  $s \in \Lambda_a, \Lambda_v$ ) satisfying the following equations:  
 2

$$\partial_t c - \nabla \cdot D(1+R)\nabla c + \nabla \cdot (\mathbf{u}_{\text{CSFC}}) + \xi(\bar{c} - \hat{c})\delta_\Gamma = 0 \quad \text{in } \Omega_{\text{CSF}}, \quad (1a)$$

$$\partial_t(\phi c) - \nabla \cdot D^*\nabla(\phi c) + \nabla \cdot (\mathbf{u}_{\text{PARC}}) + \xi(\bar{c} - \hat{c})\delta_\Gamma = 0 \quad \text{in } \Omega_{\text{PAR}}, \quad (1b)$$

$$\partial_t(A\hat{c}) - \partial_s(\hat{D}A\partial_s(\hat{c})) + \partial_s(A\hat{u}\hat{c}) + \xi P(\hat{c} - \bar{c}) = 0 \quad \text{in } \Lambda_a, \Lambda_v. \quad (1c)$$

437 In (1a),  $D$  is the (free) diffusion coefficient of the solute,  $R$  is the dispersion coefficient in the CSF spaces,  $\mathbf{u}_{\text{CSFC}}$  is the steady  
 438 CSF velocity,  $\xi$  is a permeability allowing for transfer/exchange across the interfaces  $\Gamma_a, \Gamma_v$  between the periarterial and  
 439 perivenous networks and their surroundings, the overlined  $\bar{c}$  denotes the average of  $c$  over cross-sections of  $\Gamma_a, \Gamma_v$ , and  $\delta_\Gamma$   
 440 is a Dirac term concentrated on  $\Gamma_a, \Gamma_v$ . Additionally, in (1b),  $\phi = \phi_{\text{ECS}}$  is the brain extracellular volume fraction,  $D^*$  is the  
 441 effective diffusion coefficient in the parenchyma, and  $\mathbf{u}_{\text{PAR}}$  is an interstitial fluid velocity. In this study, we set  $\mathbf{u}_{\text{PAR}} = 0$ .  
 442 In (1c),  $A = \pi(R_2^2 - R_1^2)$  is the area and  $P = 2\pi R_2$  is the perimeter of the PVS cross-sections,  $\hat{D}$  is the effective diffusion  
 443 coefficient in the PVSs, and  $\hat{u}$  is the fluid velocity (in the axial direction) in the PVS defined for the periarterial and perivenous  
 444 spaces separately ( $\hat{u}|_{\Lambda_a} = \hat{u}_a$ ,  $\hat{u}|_{\Lambda_v} = \hat{u}_v$ ). Further, we model the membrane between the parenchyma and the CSF spaces as a  
 445 semi-permeable membrane with permeability coefficient  $\beta_{\text{pia}}$ , allowing for a jump in  $c$  there. The initial concentrations in  $\Omega$   
 446 and networks  $\Lambda_a, \Lambda_v$  are all set to zero.

## 447 Molecular clearance from the intracranial space and perivascular network ends

448 We model molecular clearance, into the meningeal lymphatics or other pathways, across the upper, outer (arachnoid) boundary  
 449 (Figure 1A, Figure 2C), proportional to the concentration in the SAS with a rate constant  $\beta_{\text{exit}}$ . We set a no-flux condition at  
 450 the end nodes of the perivascular networks, not allowing for direct molecular clearance there.

## 451 Intracranial influx after intrathecal injection

452 To represent molecular influx into the intracranial compartments following intrathecal injection, without modelling the spinal  
 453 compartment explicitly, we prescribe a time-dependent molecular influx over the interface towards the spinal CSF compartment  
 454 with the condition

$$(D\nabla c - \mathbf{u}_{\text{CSFC}}) \cdot \mathbf{n} = g_{\text{influx}}, \quad \text{on } \Gamma_{\text{SSAS}}.$$

455 Here we set

$$g_{\text{influx}}(t) = \frac{m_{\text{tot}}}{T_{\text{max}}^2 |\Gamma_{\text{SSAS}}|} \max(0, T_{\text{max}} - |t - T_{\text{max}}|), \quad (2)$$

456 which expresses a hat-shaped influx function with a peak at  $T_{\text{max}}$  and a total tracer injection of  $m_{\text{tot}}$  (Table 1). We here consider  
 457 a fixed  $T_{\text{max}} = 1.0\text{ h}$  in (2), and do not consider the effect of e.g. reduced pulsatility on spinal transit time.

Parameter	Symbol	Value	Unit	Reference
Extracellular space volume fraction	$\phi_{\text{PAR}}$	0.2	–	110
Free diffusion coefficient, Gadobutrol	$D^{\text{Gad}}$	$3.8 \cdot 10^{-4}$	$\text{mm}^2/\text{s}$	111
Parenchymal diffusion coefficient, Gadobutrol	$D^{\text{Gad}}_{\text{PAR}}$	$1.2 \cdot 10^{-4}$	$\text{mm}^2/\text{s}$	79
Permeability coefficient, pia-endfoot sheath	$\beta_{\text{pia}} \xi_{\text{EF}}$	$2.6 \cdot 10^{-8}$	$\text{m/s}$	112, 92
Permeability coefficient, endfoot sheath PVS-CSF	$\xi_{\text{EF}} \xi_{\text{PVS}}$	$3.8 \cdot 10^{-7}$	$\text{m/s}$	92
Permeability coefficient, pia	$\beta_{\text{pia}}$	$2.6 \cdot 10^{-8}$	$\text{m/s}$	112
Molecular efflux rate	$\beta_{\text{exit}}$	$10^{-4} \cdot 8.0 \cdot 10^{-7}$	$\text{mm}^2/\text{m/s}$	79, *
Total molecular volume amount of injected tracer	$m_{\text{tot}}$	0.5	$\text{mmol}$	29
Molecular influx, time-to-peak	$T_{\text{max}}$	1	$\text{h}$	*
CSF production rate	$u_{\text{in}}$	0.63-0.4	1 / day	113
CSF viscosity	$\mu$	0.7	$\text{mPa}\cdot\text{s}$	114
CSF outflow resistance	$R_0 R_{\text{CSF},0}$	$10^{-5} \cdot 10^4$	$\text{Pa}/(\text{mm}\cdot\text{s})/\text{m}$	79, *
Dispersion factor, CSF spaces	$R$	†	–	*

**Table 1.** Model parameters. †/\* denotes computed/estimated within this work. The diffusion coefficient  $D^{\text{Gad}}$  represent the diffusion coefficient of Gadobutrol in CSF (water), and  $D^{\text{Gad}}_{\text{PAR}}$  its effective diffusion coefficient in human cortical tissue, both at body temperature 77, 79, 111. We use the astrocytic endfeet permeability  $\xi_{\text{EF}}$  estimated by Koch et al. 92, and we set  $\xi_{\text{PVS}} = \xi_{\text{EF}}$  as a baseline.

#### Model and material parameters

Model and material parameters are summarized in Table 1, and Table 2 gives an overview of the different in-silico scenarios. We assume that the porosity equals the extracellular space volume fraction  $\phi = \phi_{\text{PAR}}$  within the parenchyma and  $\phi = 1$  elsewhere. The effective diffusion coefficient is set equal to that of Gadobutrol in free water in the PVS networks :  $\hat{D} = D^{\text{Gad}}$ ; weighted by a  $\hat{D} = D \equiv D^{\text{Gad}}$ ; is weighted by the dispersion factor  $R$  in the CSF spaces:  $D|_{\Omega_{\text{CSF}}} = (1+R)D^{\text{Gad}}(1+R)D$ ; and modulated by the porosity and tortuosity ( $\lambda = 1.78$ ) in the parenchyma :  $D|_{\Omega_{\text{PAR}}} = D^{\text{Gad}} D^* = D^{\text{Gad}}$ . We set  $\xi$  depending on whether the PVS segment is fully embedded within the CSF spaces ( $\xi = \xi_{\text{CSR}}$ ,  $\xi = \xi_{\text{PVS}}$ ) or parenchyma ( $\xi = \xi_{\text{EF}}$ ), or neither (see also Supplementary information S1). Additionally, we increase the permeability  $\xi$  (100×) at the the To account for the unresolved continuation of the perivascular network beyond the imaging resolution limit, we implemented a permeability gradient to avoid artificial tracer buildup. At the terminal leaf nodes of  $\Lambda_a$ , permeability was increased by a factor of 100 to simulate tracer exchange with the surrounding CSF/tissue, and linearly decreasing to the baseline permeability at the next network node( $\approx 0.4 \text{ mm}$ ), to account for the transition from explicitly resolved PVSs to their unresolved continuation in the CSF spaces and parenchyma value at the adjacent network node.

#### Numerical approximation, implementation, and verification

We give a concise summary of the numerical approach here (see Supplementary methods for a comprehensive description). To solve (1) numerically, we use the interior penalty discontinuous Galerkin (DG) method with weighted averages and upwinding for the convection term in the 3D domains<sup>115</sup> – to ensure numerical stability and minimize the artificial presence of negative concentration values. For the 1D domain, we use continuous finite element spaces defined over each of the networks and stabilized with numerical diffusion when  $\hat{u}$  is non-zero. Note that the 3D–1D coupling in (1) leads to a 3D solution  $c$  with low regularity properties. Thus, one can only expect lower-order error convergence near  $\Lambda_a$  and  $\Lambda_v$ , see the references<sup>116</sup> and<sup>107</sup> for the numerical analysis of DG and continuous Galerkin schemes, respectively. However, away from these 1D networks, almost optimal approximation is expected<sup>117, 118</sup>. To numerically solve the Stokes equations to compute the CSF flow velocity and pressure in the ventricular system and SAS, we use finite element spaces that preserve the incompressibility condition on the discrete level<sup>119</sup>. This requirement is important for numerical stability when subsequently solving (1)<sup>120</sup>. The spaces we used for the velocity are continuous along the normal direction; continuity of the tangential component is enforced via interior penalty approaches<sup>119</sup>. Optimal approximation properties are expected for this scheme. These numerical methods were implemented using the FEniCS finite element framework<sup>80</sup>, and the 3D–1D coupling is handled by the extension FEniCS<sub>ii</sub><sup>81</sup>. The correctness and accuracy of the numerical solutions were verified by a series of numerical verification experiments (see Supplementary information S1.5).

The majority of the simulation time was spent on the Stokes flow and transport model simulations. Each Stokes flow simulation utilizes a hybrid parallel approach with 16 MPI processes and 4 threads each, requiring approximately 300 GB of RAM and completing in 23 minutes. The transport model is limited to serial execution by FEniCS<sub>ii</sub>, but employs 16 threads for

No.	Description $R_1, R_2$	Model description	$\xi_{\text{PVS}} = \text{CSF } \mathbf{u}_{\text{CSF}}$	$D _{\Omega_{\text{CSF}}} \hat{\mathbf{u}} _{A_a}$	$D _{\Omega_{\text{PAR}}} \hat{\mathbf{u}} _{A_m}$	$\mathbf{u} _{\Omega_{\text{CSF}}} R$	$\hat{\mathbf{u}} _{A_a} \xi_{\text{PVS}}$
0	baseline	$R_2 = 2R_1$	$\mathbf{u}_{\text{CSF}}$	$(1+R)D^{\text{Gad}} \hat{u}_a^p + \hat{u}_a^c$	$D^{\text{Gad}}_{\text{PAR}} \hat{u}_v^p$	$\mathbf{u}_{\text{CSF}} R_c + R_r$	$\hat{u}_a^p + \hat{u}_a^c$
1	no CSF production	$R_2 = 0$	$\mathbf{0}$	$-\hat{u}_a^p$	$0$	$\mathbf{0} R_c + R_r$	$\hat{u}_a^c \xi_{\text{EE}}$
2	reduced CSF pulsatility	$R_2 = R_1$	$\mathbf{u}_{\text{CSF}}$	$(1+0.1R)D^{\text{Gad}} \hat{u}_a^p + \hat{u}_a^c$	$\hat{u}_v^p$	$R_c^{\text{red}} + R_r^{\text{red}}$	$-\xi_{\text{EE}}$
3	increased CSF dispersion	$R_2 = 10R_1$	$\mathbf{u}_{\text{CSF}}$	$(1+10R)D^{\text{Gad}} \hat{u}_a^p + \hat{u}_a^c$	$\hat{u}_v^c$	$R_c^{\text{inc}} + R_r^{\text{inc}}$	$-\xi_{\text{EE}}$
4	higher PVS flow	$R_2 = R_1$	$\mathbf{u}_{\text{CSF}}$	$\hat{u}_a^p + \hat{u}_a^c + \hat{u}_a^v$	$\hat{u}_v^p$	$R_c + R_r$	$\hat{u}_a^p + \hat{u}_a^c$
5	higher PVS exchange	$R_2 = 100R_1$	$\mathbf{u}_{\text{CSF}}$	$\hat{u}_a^p + \hat{u}_a^c + \hat{u}_a^v$	$\hat{u}_v^c$	$R_c + R_r$	$-100 \xi_{\text{PVS}}$
6	dilated PVS in the SAS	$R_2 = 3R_1$	$\mathbf{u}_{\text{CSF}}$	$\hat{u}_a^p + \hat{u}_a^c + \hat{u}_a^v$	$\hat{u}_v^p$	$R_c + R_r$	$\hat{u}_a^p + \hat{u}_a^c$

**Table 2.** Overview of models and model variations. (— denotes equal to the corresponding baseline value). Each PVS cross-section is modelled as a concentric annulus with inner radius  $R_1$  and outer radius  $R_2$  and such that  $R_2 = \beta R_1$ . Let  $\xi$  denote the astrocytic endfeet permeability estimated by Koeh et al.<sup>92</sup>. The diffusion coefficients  $D^{\text{Gad}}$  represent the (free) diffusion coefficient of Gadobutrol in CSF (water), and  $D^{\text{Gad}}_{\text{PAR}}$  its effective diffusion coefficient in human cortical tissue, all at body temperature<sup>77,111</sup>.  $R$  is with color highlighting changes from the combined cardiae and respiratory dispersion enhancement field (see Methods) baseline model.  $\mathbf{u}_{\text{CSF}}$   $\mathbf{u}_{\text{CSF}}$  is the CSF velocity field induced by CSF production in  $\Omega_{\text{CSF}}$ , and  $\hat{u}_a^p$  and  $\hat{u}_v^p$  are the axial velocity velocities induced in the periarterial and perivenous networks, respectively, by the corresponding CSF pressure differences  $p_{\text{CSF}}$ . Moreover,  $\hat{u}_a^c$  and  $\hat{u}_a^v$  are the periarterial velocity velocities induced by arterial pulse wave wall motion and slow vasomotion, respectively. LastIn the model variation with no CSF production,  $\hat{u}_a^p = \mathbf{u}_{\text{CSF}} = \mathbf{0}$ ,  $p_{\text{CSF}} = 0$ , and thus  $\hat{u}_a^p = \hat{u}_v^p = 0$ .  $R_c + R_r$  is the combined cardiac and respiratory dispersion factor in the CSF spaces, with model variations  $R_c^{\text{red}}$  and  $R_r^{\text{inc}}$  corresponding to reduced pulsatility and increased pulsatility, respectively. Each PVS cross-section is modelled as a concentric annulus with inner radius  $R_1$  and outer radius  $R_2 > R_1$ . Finally,  $\hat{u}_a^p$ ,  $\hat{u}_v^p$ ,  $\hat{u}_a^c$  and  $\hat{u}_a^v$  are as  $\hat{u}_a^p$ ,  $\hat{u}_v^p$ ,  $\hat{u}_a^c$  and  $\hat{u}_a^p \hat{u}_a^v$ , respectively, but with a dilated PVS ( $R_2 = 3R_1$ ).

480 the linear system factorization, taking 22 minutes and consuming about 50 GB of memory on a AMD EPYC 9684X machine.

481

## 482 Model validation Comparison with literature results

483 As the primary means of model validation, we compare the in-silico predictions of tracer enrichment and clearance against  
484 glymphatic MRI studies (Discussion). In addition, we compare auxiliary model quantities (CSF flow rates and pressure  
485 differences, dispersion factor estimates, and the shapes and sizes of PVSs) with the current literature (see Supplementary  
486 information S2.1).

## 487 Data availability

488 Numerical simulation results generated as part of this study are openly available on Zenodo with the identifier doi: 10.5281/zenodo.14749163.  
489 This archive includes surface triangulations used for geometry representation, computational meshes (3D meshes and 1D  
490 networks), segmentations, sample simulation outputs from the baseline and high PVS flow models, and animations.

## 491 Code availability

492 The software developed to generate and analyze the numerical results of this study is openly available on Zenodo with the  
493 identifier doi: 10.5281/zenodo.14749163. In addition to simulation and analysis software, this archive also includes surface  
494 triangulations used for geometry representation, computational meshes (3D meshes and 1D networks), segmentations, sample  
495 simulation outputs from the baseline and high PVS flow models, and animations.

## 496 References

1. Rasmussen, M. K., Mestre, H. & Nedergaard, M. The glymphatic pathway in neurological disorders. *The Lancet Neurol.* **17**, 1016–1024 (2018).
2. Harrison, I. F. *et al.* Impaired glymphatic function and clearance of tau in an Alzheimer’s disease model. *Brain* **143**, 2576–2593 (2020).
3. Eide, P. K. *et al.* Plasma neurodegeneration biomarker concentrations associate with glymphatic and meningeal lymphatic measures in neurological disorders. *Nat. communications* **14**, 2084 (2023).

- 503 4. Liu, H. *et al.* Glymphatic influx and clearance are perturbed in Huntington's disease. *JCI Insight* **9** (2024).
- 504 5. Xie, L. *et al.* Sleep drives metabolite clearance from the adult brain. *Science* **342**, 373–377 (2013).
- 505 6. Eide, P. K., Vinje, V., Pripp, A. H., Mardal, K.-A. & Ringstad, G. Sleep deprivation impairs molecular clearance from the  
506 human brain. *Brain* **144**, 863–874 (2021).
- 507 7. Eide, P. K. *et al.* Altered glymphatic enhancement of cerebrospinal fluid tracer in individuals with chronic poor sleep  
508 quality. *J. Cereb. Blood Flow & Metab.* **42**, 1676–1692 (2022).
- 509 8. Miao, A. *et al.* Brain clearance is reduced during sleep and anesthesia. *Nat. Neurosci.* 1–5 (2024).
- 510 9. Hauglund, N. L. *et al.* Norepinephrine-mediated slow vasomotion drives glymphatic clearance during sleep. *Cell* **0**  
511 (2025).
- 512 10. Iliff, J. J. *et al.* A paravascular pathway facilitates CSF flow through the brain parenchyma and the clearance of interstitial  
513 solutes, including amyloid-beta. *Sci. Transl. Med.* **4**, 147ra111 (2012).
- 514 11. Ringstad, G., Vatnehol, S. A. S. & Eide, P. K. Glymphatic MRI in idiopathic normal pressure hydrocephalus. *Brain* **140**,  
515 2691–2705 (2017).
- 516 12. Louveau, A. *et al.* Understanding the functions and relationships of the glymphatic system and meningeal lymphatics.  
517 *The J. clinical investigation* **127**, 3210–3219 (2017).
- 518 13. Proulx, S. T. Cerebrospinal fluid outflow: a review of the historical and contemporary evidence for arachnoid villi,  
519 perineural routes, and dural lymphatics. *Cell. Mol. Life Sci.* **78**, 2429–2457 (2021).
- 520 14. Bohr, T. *et al.* The glymphatic system: Current understanding and modeling. *iScience* **25**, 104987 (2022).
- 521 15. Ringstad, G. *et al.* Brain-wide glymphatic enhancement and clearance in humans assessed with MRI. *JCI insight* **3**  
522 (2018).
- 523 16. Eide, P. K., Valnes, L. M., Lindstrøm, E. K., Mardal, K.-A. & Ringstad, G. Direction and magnitude of cerebrospinal  
524 fluid flow vary substantially across central nervous system diseases. *Fluids Barriers CNS* **18**, 1–18 (2021).
- 525 17. Eide, P. K., Pripp, A. H., Ringstad, G. & Valnes, L. M. Impaired glymphatic function in idiopathic intracranial  
526 hypertension. *Brain communications* **3**, fcab043 (2021).
- 527 18. Lohela, T. J., Lilius, T. O. & Nedergaard, M. The glymphatic system: implications for drugs for central nervous system  
528 diseases. *Nat. Rev. Drug Discov.* **21**, 763–779 (2022).
- 529 19. Kadan-Lottick, N. S. *et al.* Comparison of neurocognitive functioning in children previously randomly assigned to  
530 intrathecal methotrexate compared with triple intrathecal therapy for the treatment of childhood acute lymphoblastic  
531 leukemia. *J. clinical oncology* **27**, 5986–5992 (2009).
- 532 20. Eide, P. K. *et al.* Clinical application of intrathecal gadobutrol for assessment of cerebrospinal fluid tracer clearance to  
533 blood. *JCI insight* **6** (2021).
- 534 21. van Osch, M. J. *et al.* Human brain clearance imaging: Pathways taken by magnetic resonance imaging contrast agents  
535 after administration in cerebrospinal fluid and blood. *NMR Biomed.* e5159 (2024).
- 536 22. Rennels, M., Gregory, T. F., Blaumanis, O. R., Fujimoto, K. & Grady, P. A. Evidence for a ‘paravascular’ fluid circulation  
537 in the mammalian central nervous system, provided by the rapid distribution of tracer protein throughout the brain from  
538 the subarachnoid space. *Brain Res.* **326**, 47–63 (1985).
- 539 23. Zhang, E., Inman, C. & Weller, R. Interrelationships of the pia mater and the perivascular (Virchow-Robin) spaces in the  
540 human cerebrum. *J. anatomy* **170**, 111 (1990).
- 541 24. Ichimura, T., Fraser, P. A. & Cserr, H. F. Distribution of extracellular tracers in perivascular spaces of the rat brain. *Brain*  
542 *Res.* (1991).
- 543 25. Carare, R. O. *et al.* Solutes, but not cells, drain from the brain parenchyma along basement membranes of capillaries and  
544 arteries: significance for cerebral amyloid angiopathy and neuroimmunology. *Neuropathol. Appl. Neurobiol.* **34**, 131–144  
545 (2008).
- 546 26. Foley, C. P., Nishimura, N., Neeves, K. B., Schaffer, C. B. & Olbricht, W. L. Real-time imaging of perivascular transport  
547 of nanoparticles during convection-enhanced delivery in the rat cortex. *Ann. Biomed. Eng.* **40**, 292–303 (2012).
- 548 27. Hannocks, M.-J. *et al.* Molecular characterization of perivascular drainage pathways in the murine brain. *J. Cereb. Blood*  
549 *Flow & Metab.* **38**, 669–686 (2018).

- 550 28. van Veluw, S. J. *et al.* Is CAA a perivascular brain clearance disease? A discussion of the evidence to date and outlook for  
551 future studies. *Cell. Mol. Life Sci.* **81**, 239 (2024).
- 552 29. Eide, P. K. & Ringstad, G. Functional analysis of the human perivascular subarachnoid space. *Nat. Commun.* **15**, 2001  
553 (2024).
- 554 30. Yamamoto, E. A. *et al.* The perivascular space is a conduit for cerebrospinal fluid flow in humans: A proof-of-principle  
555 report. *Proc. Natl. Acad. Sci. U. S. A.* **121**, e2407246121 (2024).
- 556 31. Hadaczek, P. *et al.* The “perivascular pump” driven by arterial pulsation is a powerful mechanism for the distribution of  
557 therapeutic molecules within the brain. *Mol. Ther.* **14**, 69–78 (2006).
- 558 32. Iliff, J. J. *et al.* Cerebral arterial pulsation drives paravascular CSF–interstitial fluid exchange in the murine brain. *J.  
559 Neurosci.* **33**, 18190–18199 (2013).
- 560 33. Bedussi, B., Almasian, M., de Vos, J., VanBavel, E. & Bakker, E. N. Paravascular spaces at the brain surface: Low  
561 resistance pathways for cerebrospinal fluid flow. *J. Cereb. Blood Flow & Metab.* **38**, 719–726 (2018).
- 562 34. Mestre, H. *et al.* Flow of cerebrospinal fluid is driven by arterial pulsations and is reduced in hypertension. *Nat.  
563 communications* **9**, 4878 (2018).
- 564 35. Boster, K. A. *et al.* Artificial intelligence velocimetry reveals in vivo flow rates, pressure gradients, and shear stresses in  
565 murine perivascular flows. *Proc. Natl. Acad. Sci.* **120**, e2217744120 (2023).
- 566 36. Hirschler, L. *et al.* Region specific drivers of cerebrospinal fluid mobility as measured by high-resolution non-invasive  
567 MRI in humans. *Res. Sq.* (2024).
- 568 37. Bilston, L. E., Fletcher, D. F., Brodbelt, A. R. & Stoodley, M. A. Arterial pulsation-driven cerebrospinal fluid flow in the  
569 perivascular space: a computational model. *Comput. Methods Biomed. Eng.* **6**, 235–241 (2003).
- 570 38. Rey, J. & Sarntinoranont, M. Pulsatile flow drivers in brain parenchyma and perivascular spaces: a resistance network  
571 model study. *Fluids Barriers CNS* **15**, 20 (2018).
- 572 39. Daversin-Catty, C., Vinje, V., Mardal, K.-A. & Rognes, M. E. The mechanisms behind perivascular fluid flow. *PLoS One*  
573 **15**, e0244442 (2020).
- 574 40. Kedarasetti, R. T. *et al.* Functional hyperemia drives fluid exchange in the paravascular space. *Fluids Barriers CNS* **17**,  
575 52 (2020).
- 576 41. Gjerde, I. G., Rognes, M. E. & Sánchez, A. L. The directional flow generated by peristalsis in perivascular net-  
577 works—theoretical and numerical reduced-order descriptions. *J. Appl. Phys.* **134** (2023).
- 578 42. Nozaleda, G. L., Coenen, W., Haughton, V. & Sánchez, A. L. Arterial pulsations and transmantle pressure synergistically  
579 drive glymphatic flow. *TBA* (2024).
- 580 43. Asgari, M., De Zélicourt, D. & Kurtcuoglu, V. Glymphatic solute transport does not require bulk flow. *Sci. reports* **6**,  
581 38635 (2016).
- 582 44. Sharp, K. M., Carare, R. O. & Martin, B. A. Dispersion in porous media in oscillatory flow between flat plates:  
583 applications to intrathecal, periarterial and paraarterial solute transport in the central nervous system. *Fluids Barriers  
584 CNS* **16**, 1–17 (2019).
- 585 45. Thomas, J. H. Fluid dynamics of cerebrospinal fluid flow in perivascular spaces. *J. Royal Soc. Interface* **16**, 20190572  
586 (2019).
- 587 46. Kedarasetti, R. T., Drew, P. J. & Costanzo, F. Arterial pulsations drive oscillatory flow of CSF but not directional pumping.  
588 *Sci. reports* **10**, 10102 (2020).
- 589 47. Troyetsky, D. E., Tithof, J., Thomas, J. H. & Kelley, D. H. Dispersion as a waste-clearance mechanism in flow through  
590 penetrating perivascular spaces in the brain. *Sci. reports* **11**, 4595 (2021).
- 591 48. Martinac, A. D., Fletcher, D. F. & Bilston, L. E. Phase offset between arterial pulsations and subarachnoid space pressure  
592 fluctuations are unlikely to drive periarterial cerebrospinal fluid flow. *Biomech. Model. Mechanobiol.* **20**, 1751–1766  
593 (2021).
- 594 49. Damkier, H. H., Brown, P. D. & Praetorius, J. Cerebrospinal fluid secretion by the choroid plexus. *Physiol. reviews* **93**,  
595 1847–1892 (2013).
- 596 50. Steffensen, A. B. *et al.* Cotransporter-mediated water transport underlying cerebrospinal fluid formation. *Nat. communi-  
597 cations* **9**, 2167 (2018).

- 598 51. Liu, G. *et al.* Direct measurement of cerebrospinal fluid production in mice. *Cell reports* **33** (2020).
- 599 52. Greitz, D., Franck, A. & Nordell, B. On the pulsatile nature of intracranial and spinal CSF-circulation demonstrated by  
600 MR imaging. *Acta Radiol.* **34**, 321–328 (1993).
- 601 53. Wagshul, M. E., Eide, P. K. & Madsen, J. R. The pulsating brain: a review of experimental and clinical studies of  
602 intracranial pulsatility. *Fluids Barriers CNS* **8**, 1–23 (2011).
- 603 54. Sweetman, B. & Linninger, A. A. Cerebrospinal fluid flow dynamics in the central nervous system. *Ann. Biomed. Eng.*  
604 **39**, 484–496 (2011).
- 605 55. Fultz, N. E. *et al.* Coupled electrophysiological, hemodynamic, and cerebrospinal fluid oscillations in human sleep.  
606 *Science* **366**, 628–631 (2019).
- 607 56. Vinje, V. *et al.* Respiratory influence on cerebrospinal fluid flow – a computational study based on long-term intracranial  
608 pressure measurements. *Sci. Rep.* **9** (2019).
- 609 57. Causemann, M., Vinje, V. & Rognes, M. E. Human intracranial pulsatility during the cardiac cycle: a computational  
610 modelling framework. *Fluids Barriers CNS* **19**, 84 (2022).
- 611 58. Williams, S. D. *et al.* Neural activity induced by sensory stimulation can drive large-scale cerebrospinal fluid flow during  
612 wakefulness in humans. *PLoS biology* **21**, e3002035 (2023).
- 613 59. Zimmermann, J. *et al.* Total cerebral blood volume changes drive macroscopic cerebrospinal fluid flux in humans. *bioRxiv*  
614 2023–04 (2023).
- 615 60. Weller, R. O. Microscopic morphology and histology of the human meninges. *Morphologie* **89**, 22–34 (2005).
- 616 61. Bedussi, B. *et al.* Paravascular channels, cisterns, and the subarachnoid space in the rat brain: a single compartment with  
617 preferential pathways. *J. Cereb. Blood Flow & Metab.* **37**, 1374–1385 (2017).
- 618 62. Pizzo, M. E. *et al.* Intrathecal antibody distribution in the rat brain: surface diffusion, perivascular transport and osmotic  
619 enhancement of delivery. *The J. physiology* **596**, 445–475 (2018).
- 620 63. Mestre, H. *et al.* Periarteriolar spaces modulate cerebrospinal fluid transport into brain and demonstrate altered morphology  
621 in aging and Alzheimer's disease. *Nat. Commun.* **13**, 3897 (2022).
- 622 64. Møllgård, K. *et al.* A mesothelium divides the subarachnoid space into functional compartments. *Science* **379**, 84–88  
623 (2023).
- 624 65. Smets, N. G., van der Panne, S. A., Strijkers, G. J. & Bakker, E. N. T. P. Perivascular spaces around arteries exceed  
625 perivenous spaces in the mouse brain. *Sci. Rep.* **14**, 17655 (2024).
- 626 66. Masri, R., Zeinhofer, M., Kuchta, M. & Rognes, M. E. The modelling error in multi-dimensional time-dependent solute  
627 transport models. *ESAIM: Math. Model. Numer. Analysis* **58**, 1681–1724 (2024).
- 628 67. Hodneland, E. *et al.* A new framework for assessing subject-specific whole brain circulation and perfusion using  
629 MRI-based measurements and a multi-scale continuous flow model. *PLoS computational biology* **15**, e1007073 (2019).
- 630 68. Watts, R., Steinklein, J. M., Waldman, L., Zhou, X. & Filippi, C. G. Measuring glymphatic flow in man using quantitative  
631 contrast-enhanced MRI. *AJNR Am. J. Neuroradiol.* **40**, 648–651 (2019).
- 632 69. Causemann, M., Masri, R., Kuchta, M. & Rognes, M. E. Software and data for "In-silico molecular enrichment and  
633 clearance of the human intracranial space", DOI: [10.5281/zenodo.14749163](https://doi.org/10.5281/zenodo.14749163) (2025).
- 634 70. Deistung, A., Dittrich, E., Sedlacik, J., Rauscher, A. & Reichenbach, J. R. ToF-SWI: simultaneous time of flight and  
635 fully flow compensated susceptibility weighted imaging. *J. Magn. Reson. Imaging: An Off. J. Int. Soc. for Magn. Reson.  
636 Medicine* **29**, 1478–1484 (2009).
- 637 71. Schweser, F., Sommer, K., Deistung, A. & Reichenbach, J. R. Quantitative susceptibility mapping for investigating subtle  
638 susceptibility variations in the human brain. *Neuroimage* **62**, 2083–2100 (2012).
- 639 72. Reichenbach, J. R. The future of susceptibility contrast for assessment of anatomy and function. *Neuroimage* **62**,  
640 1311–1315 (2012).
- 641 73. Deistung, A., Schweser, F. & Reichenbach, J. R. Overview of quantitative susceptibility mapping. *NMR Biomed.* **30**,  
642 e3569 (2017).
- 643 74. Smith, A. J. & Verkman, A. S. Going against the flow: Interstitial solute transport in brain is diffusive and aquaporin-4  
644 independent. *The J. physiology* **597**, 4421 (2019).

- 645 75. Hladky, S. B. & Barrand, M. A. The glymphatic hypothesis: the theory and the evidence. *Fluids Barriers CNS* **19**, 9 (2022).
- 646 76. Betsholtz, C. *et al.* Advances and controversies in meningeal biology. *Nat. Neurosci.* 1–17 (2024).
- 647 77. Syková, E. & Nicholson, C. Diffusion in brain extracellular space. *Physiol. reviews* **88**, 1277–1340 (2008).
- 648 78. Ray, L. A., Pike, M., Simon, M., Iliff, J. J. & Heys, J. J. Quantitative analysis of macroscopic solute transport in the  
649 murine brain. *Fluids Barriers CNS* **18**, 55 (2021).
- 650 79. Hornkjøl, M. *et al.* CSF circulation and dispersion yield rapid clearance from intracranial compartments. *Front. Bioeng.  
651 Biotechnol.* **10**, 932469–932469 (2022).
- 652 80. Alnæs, M. *et al.* The FEniCS project version 1.5. *Arch. numerical software* **3** (2015).
- 653 81. Kuchta, M. Assembly of multiscale linear PDE operators. In *Numerical Mathematics and Advanced Applications  
654 ENUMATH 2019: European Conference, Egmond aan Zee, The Netherlands, September 30-October 4*, 641–650 (Springer, 2020).
- 655 82. Balédent, O. Imaging of the cerebrospinal fluid circulation. *Adult hydrocephalus* **256**, 121 (2014).
- 656 83. Gutiérrez-Montes, C. *et al.* Effect of normal breathing on the movement of CSF in the spinal subarachnoid space. *Am. J.  
657 Neuroradiol.* **43**, 1369–1374 (2022).
- 658 84. Liu, P., Owashi, K., Metanbou, S., Capel, C. & Balédent, O. Using real time phase contrast MRI to investigate CSF  
659 oscillations and aqueductal pressure gradients during free breathing. In *ISMRM 2024*, 1189 (2024).
- 660 85. van Veluw, S. J. *et al.* Vasomotion as a driving force for paravascular clearance in the awake mouse brain. *Neuron* **105**,  
661 549–561.e5 (2020).
- 662 86. Munting, L. P. *et al.* Spontaneous vasomotion propagates along pial arterioles in the awake mouse brain like stimulus-  
663 evoked vascular reactivity. *J. Cereb. Blood Flow Metab.* **43**, 1752–1763 (2023).
- 664 87. Bojarskaite, L. *et al.* Sleep cycle-dependent vascular dynamics in male mice and the predicted effects on perivascular  
665 cerebrospinal fluid flow and solute transport. *Nat. communications* **14**, 953 (2023).
- 666 88. Broggini, T. *et al.* Long-wavelength traveling waves of vasomotion modulate the perfusion of cortex. *Neuron* **112**,  
667 2349–2367.e8 (2024).
- 668 89. Coenen, W., Zhang, X. & Sánchez, A. Lubrication analysis of peristaltic motion in non-axisymmetric annular tubes. *J.  
669 Fluid Mech.* **921**, R2 (2021).
- 670 90. Jung, J.-Y., Lee, Y.-B. & Kang, C.-K. Novel technique to measure pulse wave velocity in brain vessels using a fast  
671 simultaneous multi-slice excitation magnetic resonance sequence. *Sensors* **21**, 6352 (2021).
- 672 91. Zhang, E., Richards, H., Kida, S. & Weller, R. Directional and compartmentalised drainage of interstitial fluid and  
673 cerebrospinal fluid from the rat brain. *Acta neuropathologica* **83**, 233–239 (1992).
- 674 92. Koch, T., Vinje, V. & Mardal, K.-A. Estimates of the permeability of extra-cellular pathways through the astrocyte  
675 endfoot sheath. *Fluids Barriers CNS* **20**, 1–18 (2023).
- 676 93. Bown, C. W., Carare, R. O., Schrag, M. S. & Jefferson, A. L. Physiology and clinical relevance of enlarged perivascular  
677 spaces in the aging brain. *Neurology* **98**, 107–117 (2022).
- 678 94. Bakker, E. N. T. P. *et al.* Lymphatic clearance of the brain: Perivascular, paravascular and significance for neurodegenerative  
679 diseases. *Cell. Mol. Neurobiol.* **36**, 181–194 (2016).
- 680 95. Gokina, N. I., Bevan, R. D., Walters, C. L. & Bevan, J. A. Electrical activity underlying rhythmic contraction in human  
681 pial arteries. *Circ. research* **78**, 148–153 (1996).
- 682 96. Vinje, V. *et al.* Human brain solute transport quantified by glymphatic MRI-informed biophysics during sleep and sleep  
683 deprivation. *Fluids Barriers CNS* **20**, 62 (2023).
- 684 97. Ulv Larsen, S. M. *et al.* Sleep pressure propels cerebrovascular oscillations while sleep intensity correlates with respiration-  
685 and cardiac-driven brain pulsations. *medRxiv* (2024).
- 686 98. von Holstein-Rathlou, S., Petersen, N. C. & Nedergaard, M. Voluntary running enhances glymphatic influx in awake  
687 behaving, young mice. *Neurosci. letters* **662**, 253–258 (2018).
- 688 99. Yildiz, S. *et al.* Immediate impact of yogic breathing on pulsatile cerebrospinal fluid dynamics. *Sci. reports* **12**, 10894  
689 (2022).

- 692 100. Lundgaard, I. *et al.* Beneficial effects of low alcohol exposure, but adverse effects of high alcohol intake on glymphatic  
693 function. *Sci. reports* **8**, 2246 (2018).
- 694 101. Siyahhan, B. *et al.* Flow induced by ependymal cilia dominates near-wall cerebrospinal fluid dynamics in the lateral  
695 ventricles. *J. Royal Soc. Interface* **11**, 20131189 (2014).
- 696 102. Billot, B. *et al.* Robust machine learning segmentation for large-scale analysis of heterogeneous clinical brain MRI  
697 datasets. *Proc. Natl. Acad. Sci.* **120**, e2216399120 (2023).
- 698 103. Billot, B. *et al.* Synthseg: Segmentation of brain MRI scans of any contrast and resolution without retraining. *Med. image  
699 analysis* **86**, 102789 (2023).
- 700 104. Hu, Y., Schneider, T., Wang, B., Zorin, D. & Panozzo, D. Fast tetrahedral meshing in the wild. *ACM Transactions on  
701 Graph. (TOG)* **39**, 117–1 (2020).
- 702 105. Hladky, S. B. & Barrand, M. A. Regulation of brain fluid volumes and pressures: basic principles, intracranial hypertension,  
703 ventriculomegaly and hydrocephalus. *Fluids Barriers CNS* **21**, 57 (2024).
- 704 106. Silversmith, W., Bae, J. A., Li, P. H. & Wilson, A. seung-lab/kimimaro: Zenodo release v1, DOI: [10.5281/zenodo.5539913](https://doi.org/10.5281/zenodo.5539913)  
705 (2021).
- 706 107. Laurino, F. & Zunino, P. Derivation and analysis of coupled PDEs on manifolds with high dimensionality gap arising  
707 from topological model reduction. *ESAIM: Math. Model. Numer. Analysis* **53**, 2047–2080 (2019).
- 708 108. Taylor, G. I. Dispersion of soluble matter in solvent flowing slowly through a tube. *Proc. Royal Soc. London. Ser. A.  
709 Math. Phys. Sci.* **219**, 186–203 (1953).
- 710 109. Watson, E. Diffusion in oscillatory pipe flow. *J. Fluid Mech.* **133**, 233–244 (1983).
- 711 110. Nicholson, C. & Phillips, J. Ion diffusion modified by tortuosity and volume fraction in the extracellular microenvironment  
712 of the rat cerebellum. *The J. physiology* **321**, 225–257 (1981).
- 713 111. Valnes, L. M. *et al.* Apparent diffusion coefficient estimates based on 24 hours tracer movement support glymphatic  
714 transport in human cerebral cortex. *Sci. reports* **10**, 9176 (2020).
- 715 112. Jørgen N. Riseth, K.-A. M., Timo Koch. Two-compartment modeling of tracer transport in the brain. In Rognes,  
716 M. E., Vinje, V., Dokken, J., Valnes, L. M. & Mardal, K.-A. (eds.) *MRI2FEM II: from magnetic resonance images to  
717 computational brain mechanics*, DOI: [xxxx/yyyy-zzz](https://doi.org/xxxx/yyyy-zzz) (Springer, 2025).
- 718 113. Nilsson, C. *et al.* Circadian variation in human cerebrospinal fluid production measured by magnetic resonance imaging.  
719 *Am. J. Physiol. Integr. Comp. Physiol.* **262**, R20–R24 (1992).
- 720 114. Bloomfield, I., Johnston, I. & Bilston, L. Effects of proteins, blood cells and glucose on the viscosity of cerebrospinal  
721 fluid. *Pediatr. neurosurgery* **28**, 246–251 (1998).
- 722 115. Ern, A., Stephansen, A. F. & Zunino, P. A discontinuous Galerkin method with weighted averages for advection–diffusion  
723 equations with locally small and anisotropic diffusivity. *IMA J. Numer. Analysis* **29**, 235–256 (2009).
- 724 116. Masri, R., Kuchta, M. & Riviere, B. Discontinuous Galerkin methods for 3D–1D systems. *SIAM J. on Numer. Analysis*  
725 **62**, 1814–1843 (2024).
- 726 117. Masri, R., Shen, B. & Riviere, B. Discontinuous Galerkin approximations to elliptic and parabolic problems with a Dirac  
727 line source. *ESAIM: Math. Model. Numer. Analysis* **57**, 585–620 (2023).
- 728 118. Köppl, T., Vidotto, E. & Wohlmuth, B. A local error estimate for the Poisson equation with a line source term. In  
729 *Numerical mathematics and advanced applications ENUMATH 2015*, 421–429 (Springer, 2016).
- 730 119. Hong, Q., Kraus, J., Xu, J. & Zikatanov, L. A robust multigrid method for discontinuous Galerkin discretizations of  
731 Stokes and linear elasticity equations. *Numer. Math.* **132**, 23–49 (2016).
- 732 120. Cesmelioglu, A. & Rhebergen, S. A compatible embedded-hybridized discontinuous Galerkin method for the Stokes–  
733 Darcy-transport problem. *Commun. on Appl. Math. Comput.* **4**, 293–318 (2022).

## 734 Acknowledgments

735 All authors express their gratitude to Prof. Jürgen Reichenbach for generously sharing the multi-modal human MR data, and to  
736 Prof. Erlend Hodneland for facilitating this data exchange. [The authors also thank Profs. Per Kristian Eide, Geir Ringstad and](#)  
737 [Rune Enger for valuable input and discussions.](#) M.E.R. acknowledges support from Stiftelsen Kristian Gerhard Jebsen via the  
738 K. G. Jebsen Centre for Brain Fluid Research. M.C., R.M., and M.E.R. acknowledge support from the Research Council of

739 Norway (RCN) via grant #324239 (EMIx). Simulations were performed on the Experimental Infrastructure for Exploration of  
740 Exascale Computing (eX3), which is financially supported by the RCN under contract 270053. M.K. acknowledges support  
741 from the RCN grant #303362. The figures 1A, 1D, 2C, 3C, 5A and 6A were created in Biorender.

742 **Author contributions statement**

743 M.C., M.K, R.M., and M.E.R. conceived and designed the project. M.C., M.K, R.M., and M.E.R. contributed to software  
744 development. M.C., M.K, and R.M. conducted the experiments. M.C. analyzed the results and prepared the figures. M.C.,  
745 M.K.~~and~~, R.M and M.E.R wrote the manuscript. All authors edited and reviewed the manuscript.

746 **Competing interests**

747 The authors declare no competing interests.